

INFORMATION TO USERS

This manuscript has been reproduced from the microfilm master. UMI films the text directly from the original or copy submitted. Thus, some thesis and dissertation copies are in typewriter face, while others may be from any type of computer printer.

The quality of this reproduction is dependent upon the quality of the copy submitted. Broken or indistinct print, colored or poor quality illustrations and photographs, print bleedthrough, substandard margins, and improper alignment can adversely affect reproduction.

In the unlikely event that the author did not send UMI a complete manuscript and there are missing pages, these will be noted. Also, if unauthorized copyright material had to be removed, a note will indicate the deletion.

Oversize materials (e.g., maps, drawings, charts) are reproduced by sectioning the original, beginning at the upper left-hand corner and continuing from left to right in equal sections with small overlaps. Each original is also photographed in one exposure and is included in reduced form at the back of the book.

Photographs included in the original manuscript have been reproduced xerographically in this copy. Higher quality 6" x 9" black and white photographic prints are available for any photographs or illustrations appearing in this copy for an additional charge. Contact UMI directly to order.

UMI

A Bell & Howell Information Company
300 North Zeeb Road, Ann Arbor MI 48106-1346 USA
313/761-4700 800/521-0600

Sheet-like Structures in Gravitational N-Body Simulations of the Universe

by

Jennifer L. Pauls

B.A., B.S., Bethel College, 1989

Submitted to the Department of Physics and Astronomy
and the Faculty of the Graduate School of the University
of Kansas in partial fulfillment of the requirements for
the degree of Doctor of Philosophy

Diss
1998
Diss
(Physics)

Adrian L. Melott

Adrian L. Melott, Professor & Faculty Advisor
Physics & Astronomy

Hume A. Feldman
Hume A. Feldman, Assistant Professor
Physics & Astronomy

Thomas E. Cravens
Thomas E. Cravens, Professor
Physics & Astronomy

Philip S. Baringer
Philip S. Baringer, Associate Professor
Physics & Astronomy

James R. Miller
James R. Miller, Associate Professor
Electrical Engineering & Computer Science

12/12/97
Date Defended

R00321 95019

MAY 17 1998

UMI Number: 9905468

**UMI Microform 9905468
Copyright 1998, by UMI Company. All rights reserved.**

**This microform edition is protected against unauthorized
copying under Title 17, United States Code.**

UMI
300 North Zeeb Road
Ann Arbor, MI 48103

Abstract

Jennifer L. Pauls, Ph.D.

Department of Physics & Astronomy, 1998

University of Kansas

The theme that runs through the three distinct pieces of research in this dissertation is the existence of sheet-like structures in N-body simulations of the Universe. The first topic addressed is the shape of the first objects to collapse under gravity. Many people held many differing ideas about what form these objects would tend to take - small clumps, long thin filaments, or large thin sheets. This research involved a close look at the first shapes to form in N-body simulations and concluded that the majority of the time they are sheets.

My next piece of research occupies two chapters and begins with the somewhat self-conflicting topic of "hierarchical pancaking". Pancaking describes structure formation in the Zel'dovich approximation, which is characterized by large thin sheets. Prior to this work, there were considered to be two mutually exclusive theories of structure formation. In hierarchical clustering, or "bottom-up" formation, mass collapses first into small clumps, which then are attracted into larger clumps, etc. In the pancaking model, or "top-down", mass collapses first on the largest scale, then smaller masses collapse out of those overdensities. While there are (extreme) regimes in which each of these models clearly dominates, there is a fairly wide intermediate zone which includes all reasonable models for the Universe as we observe it, for which there was no consensus. My work clearly demonstrates that this transition range is fairly smooth - with pancaking at work over the *entire* range, to greater or lesser extents. This led me to ask what quality of the Zel'dovich approximation allows it to do such a good job? The answer is that it is based on a smoothed version of the initial gravitational potential, which compares

remarkably well with the true evolved potential.

My final research involves the development of a statistic to detect sheet-like structures using the one dimensional information of the form available from quasar spectra. Using data from three closely-spaced lines-of-sight and an adapted form of the reduced three-point correlation function, I am able to detect sheets (and distinguish them from points and filaments) in toy models and N-body simulations.

Acknowledgments

I would like to first thank my advisor, Adrian Melott, who pushed me when I needed pushing and was always willing to talk through things with me.

I also would like to thank Don Lemons, who set a great example of what a professor can be and was the first person who told me I could do this. And thanks to Randy Splinter and Capp Yess who cheerfully groused along with me and then went on to set concrete examples that graduation (and even a life afterwards!) were possible.

Thanks to Tigger, for keeping me happy, bouncy, (reasonably) sane, and feeding me psari marinata.

And finally, thanks to Jon Hermes, a dear friend who was always there to hold my hand when the going got tough. (i miss you)

Contents

1	Introduction and Background	1
1.1	Scales	1
1.2	Observations	3
1.2.1	Hubble Expansion	3
1.2.2	Cosmic Microwave Background Radiation	6
1.2.3	Light Element Abundances	7
1.2.4	Dark Matter	8
1.3	The Hot Big Bang	9
1.4	Gravitational Instabilities	10
1.4.1	The Friedmann Equations	11
1.4.2	Fluid Equations	13
1.4.3	Fluid Equations in Expanding Coordinates	14
1.5	Linear Theory	15
1.5.1	Jeans Theory	16
1.6	N-Body Simulations	16
1.7	An Overview of this Work	17
1.8	References	18
2	The Zel'dovich Approximation	20
2.1	Introduction	20
2.2	The Truncated Zel'dovich Approximation	23

2.3	References	24
3	The Shape of First Collapsed Objects	25
3.1	Introduction & Background	25
3.2	The Simulations	27
3.3	Conclusions	33
3.4	References	35
4	Hierarchical Pancaking	37
4.1	Introduction	37
4.2	Comparison of the TZA with N-Body "Superpancakes"	40
4.3	Why Do Super-Pancakes Exist?	50
4.4	Conclusions	54
4.5	References	54
5	Evolution of the Gravitational Potential	56
5.1	Introduction	56
5.2	The Initial and Final Gravitational Potentials	57
5.3	Implications for Approximations	60
5.4	Conclusions	62
5.5	References	64
6	Three-Point Correlation Function and Triple Lines-of-Sight	65
6.1	Introduction	65
6.1.1	2- and 3-Point Correlation Functions	68
6.2	Method	70
6.2.1	Background	70
6.2.2	Random Coincidences	73
6.2.3	Real Coincidences	75
6.3	Results	76

6.3.1	Two-Point Correlation Function Results	76
6.3.2	Three-Point Correlation Function Results	80
6.4	References	87
7	Conclusions	88

List of Figures

1.1	A thin slice from the Las Campanas Redshift Survey showing the distribution of galaxies (each galaxy is represented by a point) centered on declination $\delta = -12^\circ$. Within the slice, the distribution is shown as a function of heliocentric velocity (redshift) and right ascension. (Shectman et al.. 1996; reprinted by permission.)	4
3.1	Projection of all the collapsed points from Simulation 1 into the xy-plane after the first time-step in which shell-crossing had occurred.	29
3.2	As in Fig. 3.1, projection into xz-plane.	29
3.3	As in Fig. 3.1, projection into yz-plane.	30
3.4	A thin slice (2 mesh units) through the center of the pancake as shown in its orientation in Figure 3.1.	31
3.5	A thin slice (2 mesh units) through the center of the pancake as shown in its orientation in Figure 3.2.	31
3.6	A thin slice (2 mesh units) through the center of the pancake as shown in its orientation in Figure 3.1, but containing all points. .	32
3.7	A thin slice (2 mesh units) through the center of the pancake as shown in its orientation in Figure 3.2, but containing all points. .	33
3.8	A thin slice (2 mesh units) through the center of the pancake as shown in its orientation in Figure 3.3, but containing all points. .	34

4.1	Thin slices taken from N-Body (left) and TZA (right) realizations with the same (random) phases with various spectral indices. The moment shown is $k_{nl} = 8k_f$; where k_f is the fundamental mode of the box. Top row: $n = -3$; second row: $n = -1$; third row: $n = +1$; bottom row: $n = +3$	38
4.2	Projections of the particles initially in a sphere chosen by the method detailed in Section 4.2. The three columns show the projections along the three eigenvectors calculated using Equation 4.1. The four rows show these projections at four stages: initial positions, $k_{nl} = 32k_f$, $k_{nl} = 16k_f$, and $k_{nl} = 8k_f$; where k_f is the fundamental mode of the box. The filaments were selected when $k_{nl} = 8k_f$. The initial spectral index is $n = -3$	43
4.3	As Figure 4.2, with $n = -1$	44
4.4	As Figure 4.2, with $n = +1$	45
4.5	As Figure 4.2, with $n = +3$	46
4.6	The ratios of longest:shortest (filled triangles) and middle:shortest (open triangles) axes for several models.	49
4.7	Cross-correlation of the smoothed N-body simulations (at $k_{nl} = 8k_f$) with the smoothed TZA against σ of the smoothed N-body density field. In decreasing order of amplitude, $n = -3$ (dot-short dash), $n = -1$ (long dashes), $n = +1$ (short dashes), and $n = +3$ (solid). The lowest line (long dash-short dash) is the cross-correlation of the $n = +3$ simulation with a linear theory extrapolation from its initial conditions and is included for comparison with the TZA performance at $n = +3$	53

5.1 The peculiar gravitational potential is shown along one diagonal of each of the four simulation cubes (a) $n = -3$, (b) $n = -1$, (c) $n = +1$, (d) $n = +3$. The units are arbitrary but do reflect that the potential is constant to linear order. Note that there is strong evolution in the potential for $n = +1, +3$, but not for $n = -3, -1$. Solid line shows the potential evolved to $k_{nl} = 8k_f$. Dotted line shows the initial potential.	58
5.2 The peculiar gravitational potential is plotted in the same manner as in Figure 5.1, except that the initial potential only has been smoothed with the same Gaussian used in the TZA (Equation 2.7). The smoothed initial potential strongly resembles the unsmoothed potential in the nonlinear regime. Note: for the case of $n = -3$, the optimal smoothing was no smoothing, so Figure 5.2a is identical to Figure 5.1a; also, the vertical scales have been changed for Figures 5.2c,d as compared with Figures 5.1c,d.	59
5.3 Plots showing the particle positions at $k_{nl} = 8k_f$ from three different models of the same initial conditions. The top row shows the Smoothed Potential: the middle shows the N-Body (for comparison); and the bottom shows the Frozen Potential. Left (right) side shows results for $n = +2$ (0) 2D models. (Melott et al., 1996: reprinted by permission.)	63
6.1 The upper two panels show spectra of the Lyman-alpha forest of the QSO pair Q1343+266 A, B. Tick marks show significant absorption features. The dotted line shows 1σ errors. The lower panel shows the observed equivalent width threshold (3.5σ) for an unresolved line as a function of wavelength for A (solid line) and B (dashed line). (Bechtold et al., 1994; reprinted by permission.)	67

6.2	Simplified sketch of three possible geometries: point/clumpy, line/filamentary, and disk/sheet-like. The lines-of-sight form a triangle (in 3D) and their intersections with the objects are marked with black dots.	68
6.3	Change in the format of the data of the 2-point correlation function. The left shows the usual data format: two differential volumes separated by a distance r . The right side shows my data format: two LOS separated by a distance S . An absorber is shown marked with a black dot. If there were an absorber in the second LOS within the window (above or below), it would be counted as a coincidence.	72
6.4	A typical picture of a double LOS with two absorbers (marked with "X"'s) along each LOS. The vertical dotted lines show the extent of the windows around each absorber. There is one hit/coincidence, which is marked.	72
6.5	An example of three LOS, with one absorber marked in the middle line.	74
6.6	An example of three LOS, with one absorber marked in the middle line. The absorbers in the upper and lower lines are each coincident with the absorber in the middle line, but not with each other. This is <i>not</i> an example of a triple coincidence.	75
6.7	The 2-point correlation function for three N-Body models. S is the separation of the LOS in cells. The range of number density of absorbers corresponds roughly to $1.5 \leq \delta \leq 16+$	77
6.8	As in Figure 6.4 for three toy models. The range of number density of absorbers corresponds roughly to $2 \leq \delta \leq 10$	78
6.9	The 3-point correlation function for three N-Body models. S is the separation of the LOS in cells. The range of number density of absorbers corresponds roughly to $1.5 \leq \delta \leq 16+$	82

6.10 A close-up of the 3-point correlation function for the three N-body models shown in Figure 6.6. The range of number density of absorbers corresponds roughly to $1.5 \leq \delta \leq 4$	83
6.11 As in Figure 6.6 for three toy models. The range of number density of absorbers corresponds roughly to $2 \leq \delta \leq 10$	84
6.12 A close-up of the 3-point correlation function for the three toy models shown in Figure 6.8. The range of number density of absorbers corresponds roughly to $2 \leq \delta \leq 6$	85

List of Tables

3.1	Information on the first collapsed objects in the simulations	28
5.1	Cross-correlation of gravitational potentials.	60
5.2	Coherence length (in cell units) of the gravitational potential for the spectral indices discussed.	61
6.1	Scales of N-body models. All distances are co-moving.	73

Chapter 1

Introduction and Background

Cosmology is the study of the large-scale structure of the Universe. There are many aspects of that study, from observation to theory to numerical modeling. All of them are closely interwoven with each other; each affecting the study of the others: observations influence theory, theory dictates the basics of modeling, modeling must produce *something* resembling the observations.... Cosmology has the distinction of being the only physical science to study a phenomena with no hope of duplicating the “experiment”. This unusual constraint forces us to effectively make predictions about the outcome *and* initial conditions of the “experiment”, based on the fairly limited picture of the Universe we are able to see today.

1.1 Scales

The natural starting point for weaving together these three components of cosmology is observations. First let’s start with a discussion of the scales of observations relevant to cosmology. Beginning rather close to home, the solar system is roughly 8×10^{14} cm across. For larger scales, astronomical convention is adopted and distances are measured in parsecs (pc). A parsec is the distance at which the orbit of the earth subtends one arcsecond; it is equal to 3.09×10^{18} cm or 3.26 light-

years. The nearest star is just over 1pc distant. Galaxies are about 10-30 kpc in diameter. M31, a nearby galaxy, is about 0.75 Mpc away. The next largest structures are clusters of galaxies. Clusters are composed of a few to a few hundred galaxies and are on the scale of 1-5 Mpc across. The nearby cluster Virgo is 21 Mpc away. Clusters can in turn be clustered themselves into superclusters which contain thousands of galaxies and are an order of magnitude larger than clusters. When we refer to the “Universe”, we nearly always mean the *visible* Universe. This is because the information it is possible to obtain about the Universe, sensitivity of instruments aside, is limited by the light-travel time. Basically, it is impossible to have information that has not had time to reach us yet. The visible Universe is roughly 3000 Mpc across.

Another very useful way to consider the observable scales of the Universe is in terms of density. A natural yardstick of density is the so-called *critical density*. Its value is $\rho_c = 3H^2/8\pi G$ where H is the Hubble constant which describes how fast distant objects are receding from us due to the expansion of the Universe and G is Newton's gravitational constant. The ultimate fate of the Universe rests on its density. If the density is below ρ_c , the Universe is called “open” and will expand forever. Its geometry will be the 3D analog of the surface of a saddle shape. If the density is above ρ_c , then the Universe is called “closed” and will eventually halt its expansion and recollapse in a big crunch. In this case, the geometry is the 3D analog to the surface of a sphere. The density which separates these two cases is aptly named the critical density – if the Universe has this density, it is termed “flat” and will expand forever, but the rate of expansion will asymptotically approach zero. This corresponds to normal Euclidean geometry. There has been a great deal of controversy about the exact value of H , and it will be discussed further in the next section, but for order of magnitude estimates, let us assume that $H \sim 75 \text{ km/s/Mpc}$, so that $\rho_c \sim 1 \times 10^{-29} \text{ g/cm}^3$ or about 10 protons per cubic meter. Water has a density of $1 \text{ g/cm}^3 = 1 \times 10^{29} \rho_c$. Galaxies have roughly

a density of $5 \times 10^{-24} g/cm^3 = 5 \times 10^5 \rho_c$, while clusters and superclusters have even lower mean densities of $\sim 10^3 \rho_c$. The best estimates for the Universe as a whole puts its density at $\sim 0.03 - 1 \rho_c$. It is customary to refer to density by the dimensionless parameter Ω , which represents a fraction of the closure density: $\Omega = \rho/\rho_c$.

The smallest scale of objects (existing in the present) that most cosmologists deal with is galaxies. In simulations, it is common to have point masses roughly on the mass scale of galaxies and the simulation box size roughly on the scale of superclusters of galaxies. So, for the most part, cosmologists are not interested in “tiny” things like solar systems, globular clusters, or internal details of galaxy structure.

Figure 1.1 shows galaxies in a thin slice through the Universe taken from the Las Campanas Redshift Survey (Shectman et al., 1996). This slice is on the same scale as a slice through the simulations used in this paper.

1.2 Observations

1.2.1 Hubble Expansion

Just as the wavelength of sound emitted from a moving source is Doppler shifted and detected at a different wavelength, so the wavelength of light emitted from a moving source is shifted as well. If the source is moving towards an observer, the light is detected at a shortened wavelength and is thus said to be blueshifted. If, as is more commonly the case in extra-galactic observations, the source is moving away, the light is detected at a longer wavelength and is called redshifted. The relationship between the velocity of the source and the emitted and detected wavelengths is:

$$z = \frac{\lambda - \lambda_0}{\lambda_0} = \frac{v}{c} \quad (1.1)$$

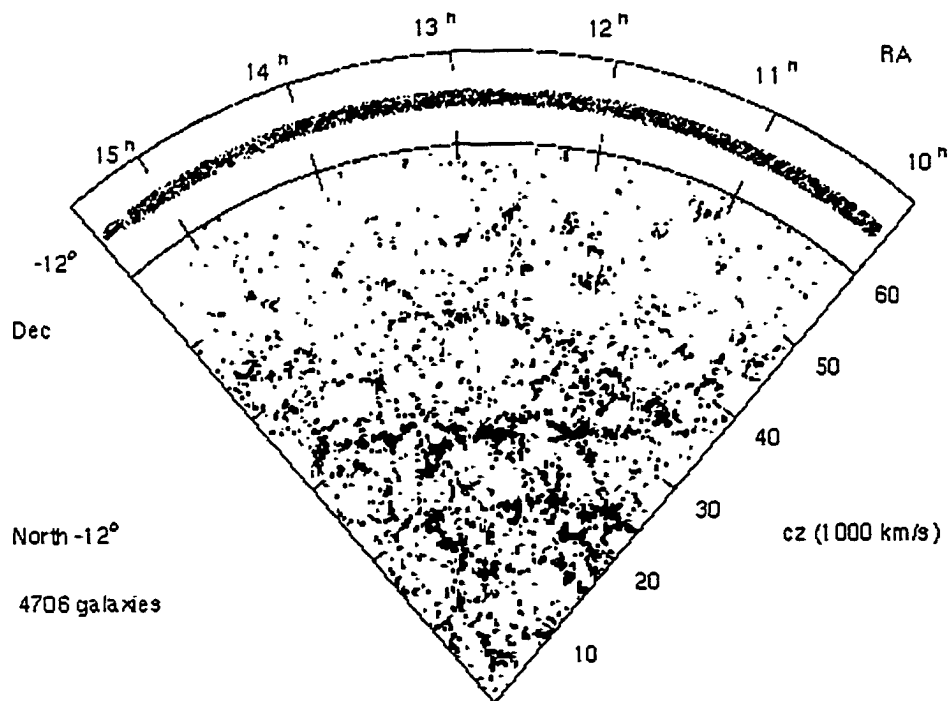


Figure 1.1: A thin slice from the Las Campanas Redshift Survey showing the distribution of galaxies (each galaxy is represented by a point) centered on declination $\delta = -12^\circ$. Within the slice, the distribution is shown as a function of heliocentric velocity (redshift) and right ascension. (Shectman et al., 1996; reprinted by permission.)

where λ is the detected wavelength, λ_0 is the emitted wavelength, v is the relative radial velocity of the source, c is the speed of light, and z is the “redshift” of the source.

In the 1920's a revolution of sorts occurred in cosmology when Slipher and Hubble made the redshift observations that led Hubble to write the now famous equation $v = H_0 D$. This equation uses Hubble's constant, H_0 , to relate the velocity v with which an object is receding to its distance D from the observer. The linearity of this relationship lead to the realization that not only is the Universe expanding, but it is expanding from every point. That is, we do not occupy a special position in the Universe and all observers should see the same recession behavior. The accepted value of H_0 has been dramatically lowered since Hubble's original estimate, although today there is still quite a lot of uncertainty in it. To allow for that, the convention is to write $H_0 = 100 h_0 \text{ km/s/Mpc}$, where h_0 is a dimensionless quantity representing our uncertainty. Currently it is believed that $0.4 \leq h_0 \leq 1.0$, far lower than Hubble's original estimate of $h_0 \sim 5$.

As a result of this expansion, objects at large distances appear to be receding from us at roughly the velocities dictated by the Hubble law. There are deviations, called peculiar velocities, due to gravitational clustering, but on large scales (larger than galaxy clusters), velocities due to the Hubble expansion dominate. Because of this, the redshift is sometimes used to describe the (approximate) distance to an object. Also, since looking at distant objects is effectively looking back in time (due to the finite speed of light), the redshift can also be used to describe when an event occurred, or the earliest time a type of object is observed to exist.

This observation of expansion from every point was perhaps the first clue that the Cosmological Principle is a reasonable approximation of the Universe. The Cosmological Principle states that the Universe is homogeneous and isotropic. Homogeneity means that Universe looks the same from all vantage points. The form of Hubble's Law requires that each point see the same recession law – that is,

the expansion is homogeneous. Isotropy means that the Universe looks the same in all directions. Now clearly the Universe is not *totally* isotropic – the sun is not seen in all directions, the plane of the Milky Way can be discerned, and there are such large-scale objects as the Great Attractor which are not repeated across the sky. However, on sufficiently large scales the distribution of voids, clusters, super-clusters, filaments, and sheets of galaxies is fairly smooth. While there is no way to empirically verify the Cosmological Principle, it does seem a reasonable and minimal starting point for mathematical and theoretical descriptions of the Universe.

1.2.2 Cosmic Microwave Background Radiation

The discovery of the Cosmic Microwave Background Radiation (CMBR) was an even stronger argument for the Cosmological Principle. In 1965 Penzias and Wilson, two engineers working for Bell Labs, discovered uniform background radio noise at microwave frequencies. They tried to identify the source, but determined the radiation was completely uniform, ruling out terrestrial, solar, and galactic sources. Happily, word of their strange discovery reached Robert Dicke and his collaborators (1965) at nearby Princeton, who were independently redoing some work originally conceived by George Gamow (1946). That work dealt with the creation of nuclei (deuterium, helium, etc.) in the early Universe through nuclear fusion which necessarily occurred at very high temperatures $\sim 10^9 K$. Their theory predicted a radiation background would be created during this nucleosynthesis era and that radiation would have a blackbody spectrum characterized by the temperature at which nucleosynthesis occurred. During nucleosynthesis and for a time afterwards, matter and radiation remained in equilibrium and interacted with each other. As the Universe expanded, it cooled and eventually reached a temperature at which the photons could no longer pair-produce or ionize atoms. At this time, matter and radiation ceased interacting and continued their evolution

and cooling separately. From this point, gravity dominates the evolution of the matter, and the radiation background is left virtually “intact”. In the time since this decoupling, the radiation background has cooled with the expansion of the Universe (that is, the photons redshift) until today the characteristic temperature of this radiation should be a few Kelvins. In fact, the radiation discovered by Penzias and Wilson has a near-perfect black-body spectrum with a temperature of 2.73K. Their discovery lead to the Nobel Prize in Physics in 1978.

Since the CMBR presents a sort of “snapshot” of the Universe at the time of recombination, observations of it can tell us a lot about the size of density perturbations at that time. From the time of its discovery in the mid-60’s until the data from the COBE satellite hit the front pages of newspapers in 1990, the CMBR kept cosmologists guessing. Most everyone believed that fluctuations had to be there, but the scale was elusive. The fluctuations had to be large enough to produce the structure observed today, and the ability of gravitational instability (the favored mechanism) to create galaxies, superclusters, etc. in the time available was being pushed to the limit by observations that put tighter and tighter constraints on the size of the CMBR perturbations. Cosmologists breathed a collective sigh of relief when perturbations were finally announced (Smoot et al., 1992). Any serious model of structure formation must now be capable of taking perturbations no larger than those discovered by the COBE team, and producing the structures we see today.

1.2.3 Light Element Abundances

In the early part of this century it was believed that all elements heavier than hydrogen were produced in stellar interiors. However, in the 1940’s, it was realized that there was much more helium present than could be explained with standard stellar nucleosynthesis. Alpher, Bethe, & Gamow (1948) responded by developing the idea of cosmological nucleosynthesis, in which light nuclei were formed in a very

early hot phase of the Universe. The original model produced too much helium, until Alpher & Herman (1948) suggested that there might be an accompanying background of radiation which would cause some of the helium to be broken down. They predicted that this radiation would have cooled to about 5 K by the present day (amazingly near the 2.73 K detected over fifteen years later).

More modern theoretical work is able to estimate the relative numbers of neutrons and protons (about 1:7) in the very early Universe and use that ratio, along with knowledge of binding energies of various nuclei to predict the relative abundances of the light elements. One of these ratios is the mass in ^4He to the mass in ^1H and ^4He which is usually written $Y_4 \simeq 0.25$. The best estimates of Y_4 from observational data put it in the range 0.22-0.24, with no directional dependence (Roos 1997). Such agreement of cosmological nucleosynthesis theory and observations offer convincing explanations of current light element abundances, and provide strong support of the Big Bang theory.

1.2.4 Dark Matter

Observers developed techniques for “weighing” galaxies, based upon their rotation curves. That is, using Keplerian dynamics, the speed of objects near the visible edges of galaxies was used to determine the total mass that their orbits must encircle, which was assumed to be the total mass of the galaxy. However, in the 70’s velocity measurements were taken of objects, hydrogen clouds in at least one study (Roberts & Whitehurst 1975), much farther out than the luminous edge. It was discovered that these objects were moving at roughly the same speed as the objects near the luminous edge. The dynamical conclusion of this observation is that the galaxies must contain mass beyond the visible edge – mass that has come to be known as “dark matter” because it is only visible through its gravitational effects. A few years later, a series of optically-based rotation curve observations were undertaken by Rubin, Ford, & Roberts (1979 and references

therein) which led to the same conclusions. Dark matter has also been found to affect the dynamics of gravitationally bound clusters in much the same way.

Currently dark matter is a mystery – there are many theories about what it could (and could not) be, but there is not yet enough evidence to settle the debate. Dark matter is usually spoken of as being “hot” or “cold” or a mixture of the two. “Hot” describes matter that was relativistic at the time of decoupling, and therefore has a large velocity dispersion while “cold” describes matter which was non-relativistic at decoupling and so has a small velocity dispersion. Structures that form out of hot dark matter (HDM) tend to form on the largest scales first, and then fragment into smaller objects. Cold dark matter, on the other hand, forms first into small clumps, which then gravitate into larger and larger structures. A standard candidate for HDM is a low-mass (on order of 10 eV) neutrino. There are several theoretical candidates for CDM such as WIMPs (weakly interacting massive particles), axions, or photinos, as well as objects known to exist, but which are unlikely to be prevalent enough to account for all the dark matter, such as non-luminous Jupiter-sized objects. Another aspect to the debate is whether the dark matter is baryonic or non-baryonic. Nucleosynthesis constrains quite tightly the total amount of baryonic matter (matter composed of baryons, which are primarily protons and neutrons) produced in the early Universe to $0.010 \leq \Omega_b h^2 \leq 0.015$ (Coles & Lucchin 1995). Current best estimates indicate that there is much more mass in the Universe ($\Omega \sim 0.3$) than is possible due to baryons alone – therefore at least some of the dark matter must be non-baryonic.

1.3 The Hot Big Bang

The above observations are merged in the theory called the Hot Big Bang. Grounded in General Relativity via the Friedmann equations, the Hot Big Bang incorporates the Hubble expansion as a natural consequence of the mathematics. Running the

expansion “backwards”, it is easy to imagine the Universe becoming much smaller, denser, and hotter. The extremely high temperatures of the early Universe are sufficient for the fusion of cosmological nucleosynthesis, resulting in the abundances of light elements observed today. As well, the cooling that comes with expansion reduces the temperature of the relic CMBR photons to the 2.73 K blackbody that is observed today.

There are a few things left unexplained by the Hot Big Bang, and some people entertain alternate theories of how the Universe came to be the way it is (see Coles & Lucchin (1995) for an overview). However, on the whole the Hot Big Bang explains (and has *predicted*) more of the features of the Universe than do the other theories and it is currently accepted by most scientists as the best working theory.

1.4 Gravitational Instabilities

It is a generally accepted view that the structures we see in the Universe today formed through gravitational collapse. The other forces are either short-range (strong and weak nuclear) or effectively short-range (electro-magnetic) because matter has always been electrically neutral on all but the very tiniest scales. The basic outline of how structures are believed to have formed begins with tiny (quantum) perturbations around the time of recombination ($z \sim 1100$) when the Universe was only 100,000 years old. Before this time matter and radiation were in equilibrium, their motions dominated by electro-magnetic interactions, and perturbations could not grow. Once matter became neutral at recombination, gravity became the dominant force and perturbations were able to grow. It is believed that the form of these perturbations is “written” on the CMBR, which explains the flurry of excitement surrounding the detections anisotropies in it. The tiny overdense regions attract matter away from other tiny underdense regions. Eventually, some of the overdense regions become dense enough that they collapse

and become gravitationally bound. As the Universe evolves, these collapsed regions keep getting denser and denser and the underdense areas get more and more underdense.

1.4.1 The Friedmann Equations

In order to proceed farther in the discussion of the growth of gravitational instabilities, a mathematical framework must be introduced (see, for example, Coles & Lucchin 1995). General Relativity provides that framework in the form of the Einstein equations:

$$R_{ij} - \frac{1}{2}g_{ij}R - \Lambda g_{ij} = \frac{8\pi G}{c^4}T_{ij} \quad (1.2)$$

where i and j run from 0 to 3, R_{ij} is the Ricci tensor, R is the Ricci scalar, Λ is the cosmological constant (if present), g_{ij} is the metric tensor, and T_{ij} is the energy-momentum tensor. Einstein originally added the Λ term to allow a static solution to these equations before the expansion of the Universe had been detected. While Einstein later dubbed it his greatest error, there has recently been interest in reviving this term. A positive value of Λ acts like a negative energy density – a force driving expansion. The Λ term is necessarily quite small – if it were not, we would expect to see random motions of galaxies much like the random motions of the molecules of a gas under pressure. It is included here as a formality – none of the results presented in later chapters depend upon it. The energy-momentum tensor which is most appropriate is that of a perfect fluid, $T_{ij} = (p + \rho c^2)U_i U_j - p g_{ij}$, where p is the pressure, ρc^2 is the energy density (which includes the rest energy), and U_k is the fluid 4-velocity.

Now a metric must be introduced. In General Relativity, the metric describes, four dimensionally, the geometry of space-time. In order to describe the Universe properly, the metric must allow for Hubble expansion, and, since we do not yet know whether the Universe is open, closed, or at critical density, should allow for

any of these options. Those criteria are satisfied by the Robertson-Walker metric:

$$ds^2 = (c dt)^2 - a(t)^2 \left[\frac{dr^2}{1 - \kappa r^2} + r^2(d\theta^2 + \sin^2\theta d\phi^2) \right], \quad (1.3)$$

where ds is a differential space-time path element, $a(t)$ is the cosmological scale factor which describes how fast the Universe is expanding, r, θ, ϕ are spherical coordinates in the expanding system, and κ is a parameter describing the curvature. If the Universe is open, $\kappa = -1$, if it is closed, $\kappa = +1$, and if it has critical density, $\kappa = 0$.

Applying the Einstein equations to the Robertson-Walker metric gives the Friedmann equations. The first equation is basically the conservation of energy:

$$H_0^2 = \left(\frac{\dot{a}}{a} \right)^2 = \frac{8\pi G}{3}\rho + \frac{\Lambda}{3} - \frac{\kappa c^2}{a^2}, \quad (1.4)$$

where a dot above a variable indicates the time derivative. The left-hand term represents the kinetic energy, the left term on the right-hand side represents potential energy. the Λ term acts like a kinetic energy, and the remaining term records whether expansion (open) or energy density (closed) dominates. The next Friedmann equation describes the balance of forces:

$$\frac{\ddot{a}}{a} = \frac{-4\pi G}{3c^2}(\rho c^2 + 3p) + \frac{\Lambda}{3}. \quad (1.5)$$

And the final Friedmann equation is based upon universal expansion being adiabatic:

$$\dot{\rho} = \frac{-3\dot{a}}{a} \left(\frac{p}{c^2} + \rho \right). \quad (1.6)$$

It is from Equation 1.4 that the critical density is defined. Since the critical density is that which separates open and closed universes, it is characterized by $\kappa = 0$. In the (usual) case where Λ is assumed to be zero, it is easy to solve and show that $\rho_c = 3H^2/8\pi G$. In the special case of an $\Omega = 1$ matter-dominated universe, these

equations can be used to give the time dependence of the scale factor: $a(t) \propto t^{2/3}$ or $a(t) = a_0 (t/t_0)^{2/3}$.

In general, the Friedmann equations are used for theoretical work – getting an expression for the critical density, describing the growth of perturbations within different models (i.e. matter- or radiation-dominated, different values of Ω , etc.) of the universe and the like. The framework for most actual simulations is laid out by the fluid equations, although some simulations are carried out wholly or in part by calculating the direct 2-body interactions using Newton's law of gravitation.

1.4.2 Fluid Equations

The fluid equations are derivable from the Vlasov equation which is the collisionless form of the Boltzmann equation:

$$\frac{df}{dt} = \frac{\partial f}{\partial t} + \frac{\mathbf{p}}{ma^2} \cdot \nabla f - m\nabla\phi \cdot \frac{\partial f}{\partial \mathbf{p}} = 0, \quad (1.7)$$

where $f = f(\mathbf{x}, \mathbf{p}, t)$ is the particle distribution function, \mathbf{p} is the momentum, m is the particle mass, and ϕ is the gravitational potential. The fluid equations are obtained by multiplying the Vlasov equation by products of the momentum components and integrating over momentum (Bouchet 1996).

Assuming it is safe to treat the contents of the Universe as a self-gravitating fluid, the motion of matter can be described in terms of three fluid equations. The first is the continuity equation:

$$\frac{\partial \rho}{\partial t} + \vec{\nabla} \cdot (\rho \mathbf{u}) = 0, \quad (1.8)$$

where ρ is the density and \mathbf{u} is the (local) velocity. This equation guarantees that mass is neither created nor destroyed in the system. The next is the Euler equation which basically shows the balance of forces:

$$\frac{\partial \mathbf{u}}{\partial t} + (\mathbf{u} \cdot \vec{\nabla}) \mathbf{u} + \frac{1}{\rho} \vec{\nabla} p + \vec{\nabla} \phi = 0. \quad (1.9)$$

The pressure is p , ϕ is the gravitational potential, and time is t . And finally the Poisson equation:

$$\nabla^2 \phi = 4\pi G \rho \quad (1.10)$$

which describes gravity as a conservative field, derived from the potential ϕ which is determined by the distribution of mass. Viscosity and thermal conductivity terms have been ignored.

1.4.3 Fluid Equations in Expanding Coordinates

With Hubble's discovery, the above fluid equations needed to be reworked to include the effects of expansion. Taking the Universe to be expanding with the scale factor $a(t)$ (from this point, the time-dependence of a will not be written explicitly), these equations may be rewritten in terms of the co-moving coordinate $\mathbf{x} = \mathbf{r}/a$, where \mathbf{r} is the "proper" coordinate. In this form, the co-moving separation of two points whose relative velocity is due *only* to expansion will not change with time. Their proper separation, however, will grow. Thus, the proper velocity is written: $\mathbf{u} = \dot{a}\mathbf{x} + \mathbf{v}(\mathbf{x}, t)$. The term $\dot{a}\mathbf{x}$ is the Hubble flow (velocity due to the expansion of the Universe) and $\mathbf{v} = a\dot{\mathbf{x}}$ is the peculiar velocity – the velocity with respect to the co-moving coordinate system. The convention of expressing the density as a density contrast is also introduced:

$$\delta(\mathbf{x}, t) = \frac{\rho(\mathbf{x}, t) - \bar{\rho}(t)}{\bar{\rho}(t)}, \quad (1.11)$$

so that

$$\rho(\mathbf{x}, t) = \bar{\rho}(t)(1 + \delta(\mathbf{x}, t)). \quad (1.12)$$

$\bar{\rho}$ is the mean mass density of the Universe and has the very simple time dependence $\bar{\rho}(t) = \bar{\rho}(t_0) \times (a_0/a(t))^3$ in the matter-dominated phase of the Universe, which is the time of interest for this work.

The continuity equation thus becomes:

$$\frac{\partial \delta}{\partial t} + \frac{1}{a} \vec{\nabla} \cdot ((1 + \delta) \mathbf{v}) = 0. \quad (1.13)$$

Where the gradient is now with respect to co-moving coordinates and is related to the proper gradient by $\vec{\nabla} = a \vec{\nabla}_{proper}$. The Euler equation becomes:

$$\frac{\partial \mathbf{v}}{\partial t} + \frac{\dot{a}}{a} \mathbf{v} + \frac{1}{a} (\mathbf{v} \cdot \vec{\nabla}) \mathbf{v} + \frac{c_s^2}{a} \vec{\nabla} \delta + \frac{1}{a} \vec{\nabla} \phi = 0 \quad (1.14)$$

where $c_s = (dp/d\rho)^{1/2}$ is the speed of sound. The potential in the Poisson equation is redefined using the density contrast δ :

$$\nabla^2 \phi = 4\pi G \bar{\rho} a^2 \delta. \quad (1.15)$$

This prevents divergence of the potential (Peebles 1980). Writing the potential this way is the same as adding an overall constant to assure that $\int \phi d^3x = 0$. These equations as they stand are non-linear and have no full analytic solution. There are three common ways to handle these equations: linear theory, N-body simulations, and the Zel'dovich approximation. The two which shall be used in this paper are computational N-body methods and the Zel'dovich approximation.

1.5 Linear Theory

The simplest approximate solution to the above equations (1.13 - 1.15) is obtained from first-order perturbation theory (e.g. see Peebles 1980). If the density is approximated $\rho = \bar{\rho}(1 + \delta)$ and the pressure term is dropped, then there are two solutions – one growing and one decaying in time. Only the growing mode is

important for structure formation. In general, the density contrast is described by:

$$\frac{\partial^2 \delta}{\partial t^2} + 2\frac{\dot{a}}{a}\frac{\partial \delta}{\partial t} = 4\pi G\bar{\rho}\delta. \quad (1.16)$$

For the special case of $\Omega = 1$, the solution is $\delta(\mathbf{x}, t) = a(t)\delta(\mathbf{x}, t_i)$ for the growing mode. (The decaying mode dies out as $\propto t^{-1}$.)

1.5.1 Jeans Theory

Jeans theory was developed by Sir James Jeans in the early part of the 20th century in an attempt to explain the formation of stars and planets using gravitational instability. Very basically, there are two forces at work on an overdense region - gravity which tends to collapse, and pressure which tends to expand. Since pressure is proportional to density, the more gravity acts to increase density, the more pressure acts to reduce it. The main thrust of Jeans Theory is to find the interesting points which separate the cases when gravity dominates and gravitational collapse occurs and when pressure dominates and there are oscillating sound waves but no gravitational collapse. Very approximately, gravitational collapse will occur when the size of the overdense perturbation is greater than the Jeans length: $\lambda_J = v_s(G\rho)^{-1/2}$ where v_s is the velocity of sound and ρ is the average density. The time it will take to collapse is then roughly $(G\rho)^{-1/2}$.

1.6 N-Body Simulations

The N-body simulations used in this paper are all created using staggered Particle-Mesh (PM) codes with periodic boundary conditions and 128^3 particles on a mesh of 128^3 grid cells. Grid-based methods have the benefit of being able to handle a large number of particles quite efficiently, but in doing so, one pays a price in resolution. The Nyquist frequency is an upper limit on wavenumbers which can be

resolved: $k_{Ny} = 64k_f$ where k_f is the fundamental mode of the box. This means that there is a smallest wave/scale that can be resolved, and structure that occurs on scales smaller than $\sim k_{Ny}^{-1}$ should not be assumed to be correct. PM codes work by using the particles to create a density field on the mesh. This density field is Fourier transformed (using an FFT), the potential is found in k-space by solving the Poisson equation, and transformed back. Then the acceleration on the grid points is found by differencing the real-space potential and the acceleration at each mass point is found through interpolation. These accelerations are used to update the particles' positions and velocities, and the process is repeated.

The power spectrum is formally defined as $P(k) = \langle |\delta_k^2| \rangle$, where δ_k are the elements of the Fourier transform of the density distribution. The initial perturbations used in the simulations in this paper have power law power spectra $P(k) \propto k^n$ with random phases and are imposed using the Zel'dovich approximation (Chapter 2) at a sufficiently low amplitude that evolution begins well within the linear regime. In most cases, the evolution is allowed to continue until $k_{nl} = 8k_f$ where k_{nl} is the wavenumber just becoming non-linear as defined by $\delta^2 = 1 = a^2 \int_0^{k_{nl}} P(k) d^3k$. Power law power spectra (when there are no constraints on allowable wavenumbers, such as Nyquist frequency cutoffs) are scale-free, which means that stopping the simulation at different times does not affect the appearance of the structures, just their relative scales. However, this is not quite true in real simulations, and stopping the evolution at $k_{nl} = 8k_f$ strikes a good balance – fitting the characteristic structure size well between the resolution limit and the size of the box.

1.7 An Overview of this Work

It has only been within the last seventy years or so that modern cosmology has come into existence, and we are just beginning to get a sense of what the large-scale structure of our Universe looks like. This work attempts to add to that

understanding by studying how, when, and why a certain type of structure, large sheets, forms. This first chapter has discussed some general background cosmology and gives the framework in which this research fits. Chapter 2 discusses the Zel'dovich approximation (ZA), which has sheets, or "pancakes", as a natural consequence of the form of the approximation. The ZA is useful both because it is a remarkably accurate and efficient approximation and because it can be studied to see what aspect of the limited physics on which it is based is responsible for its accuracy and the formation of sheets.

In Chapter 3 I investigate the shapes the first objects to collapse under gravity. This work involved a close look at the first shapes to form in N-body simulations and concluded that the majority of the time they are sheets.

Chapters 4 and 5 both deal with the relationship of the ZA pancakes to structures visible in N-body simulations. In Chapter 4 I show that there is a real correlation between the pancakes seen in the ZA and structures seen in N-body simulations with a wide range of initial conditions. In Chapter 5 I go farther and analyze *why* these structures are the same.

Chapter 6 details my development of a new statistic capable of detecting sheets using sets of 1D data, such as Lyman-alpha lines from quasar spectra. The statistic is a variation of the reduced three-point correlation function and is useful because there are some types of matter which cannot be directly (visually) observed, but must be seen using background light.

The final chapter, Chapter 7, is a summary of the results of this dissertation, and a look at the implications of it for future work.

1.8 References

Alpher R. A. & Herman R. C. 1948, Nature, 162, 774

Alpher R. A., Bethe H. A., & Gamow G. 1948, Phys. Rev., 73, 803

- Bouchet F. R. 1996, from *Proceedings of the International School of Physics "Enrico Fermi"* Course CXXXII, eds Bonometto S., Primack J. R., & Provenzale A., (Amsterdam: IOS Press), 565-599
- Coles P. & Lucchin F. 1995, *Cosmology the Origin and Evolution of Cosmic Structure*, (Chichester: John Wiley & Sons)
- Dicke R. H., Peebles P. J. E., Roll P. G., & Wilkinson. D.T. 1965, Ap.J. 142, 414
- Gamow G., 1946 Physical Review, 70, 572
- Mather J. C., et al. 1990, ApJ, 354, L37
- Peebles P. J. E. 1980, *The Large-Scale Structure of the Universe*, (Princeton: Princeton University Press)
- Penzias A. A. & Wilson R. W. 1965, ApJ, 142, 419
- Roberts M. S. & Whitehurst R. N. 1975, ApJ, 201, 327
- Roos M. 1997. *Introduction to Cosmology*. (Chichester: John Wiley & Sons)
- Shectman S. A.. Landy S. D., Oemler A., Tucker D. L., Lin H.. Kirshner R. P., & Schechter P. L. 1996, ApJ, 470, 172
- Smoot G. F. et al. 1992, ApJ, 396, L1

Chapter 2

The Zel'dovich Approximation

2.1 Introduction

The Zel'dovich Approximation (ZA) is a first order approximation to gravitational instability in a pressureless, collisionless, continuous medium first proposed by Zel'dovich in 1970. In this approximation, structures form in characteristic Zel'dovich "pancakes" – thin sheet-like structures. Because this paper focuses on sheets, it is useful to consider how structures form in the ZA, as well as direct comparisons of these structures with those formed in n-body simulations. The equation itself is of a quite simple form:

$$\mathbf{r}(\mathbf{q}, t) = a(t)\mathbf{q} + b(t)\nabla S(\mathbf{q}) \quad (2.1)$$

Where \mathbf{q} is the particle's initial (Lagrangian) position, $a(t)$ is the cosmological scale factor, $b(t)$ is a known function for a given value of Ω , $S(\mathbf{q})$ is the initial peculiar velocity potential (the potential field from which the initial, irrotational, peculiar velocities may be derived), and \mathbf{r} is the particle's (Eulerian) position at time t . Here one can get a good sense of the physical motivation of the approximation. The particle's final position is based on two kinds of motion: $a(t)\mathbf{q}$ is just the motion due to the Hubble expansion and $b(t)\nabla S(\mathbf{q})$ is the motion due

to inhomogeneities in the density field. However, the velocity is constant and the time dependence is such that the particle will not be able to stop and become bound in a clump – the point at which a particle crosses paths with another particle is the point at which the ZA breaks down for those two particles. Thus, pressure/collisionality are not modeled by this approximation.

For $\Omega = 1$, $S(\mathbf{q})$ can be simply related to the initial peculiar gravitational potential, ϕ :

$$\phi(\mathbf{q}) = -\frac{3}{2} H^2 a^3 S(\mathbf{q}). \quad (2.2)$$

The source term for ϕ in the Poisson equation is $\delta = \frac{\rho - \bar{\rho}}{\bar{\rho}}$, rather than ρ , to prevent divergence (Peebles 1980). For $\Omega \neq 1$ a somewhat more complicated relationship may be derived (see, for example, Sahni & Coles 1995). This approximation can also be written in co-moving coordinates (again with $\Omega = 1$, which leads to $b = a^2$):

$$\mathbf{x}(\mathbf{q}, t) = \mathbf{q} + a(t) \nabla S(\mathbf{q}). \quad (2.3)$$

where \mathbf{x} is the particle's co-moving position at time t .

The initial (Lagrangian) density is constant throughout space, while density is position-dependent in Eulerian space. The Jacobian of the transformation between Lagrangian and Eulerian space can be used to relate the two:

$$\rho(\mathbf{q}, t) = \bar{\rho}_L \left(\frac{d\mathbf{r}}{d\mathbf{q}} \right)^{-1} \quad (2.4)$$

The factor $\left(\frac{d\mathbf{r}}{d\mathbf{q}} \right)$ is a tensor and is called the *deformation tensor* because it describes the way Lagrangian space deforms into Eulerian space.

The deformation tensor elements can be written at each particle:

$$d_{ik} = \frac{\partial x_i}{\partial q_k} = \delta_{ik} + a(t) \frac{\partial (\nabla S(\mathbf{q}))_i}{\partial q_k}. \quad (2.5)$$

The eigenvectors of this tensor give the principle directions of collapse (or expansion) about a particle and the corresponding eigenvalues imply the time at which there will be infinite compression along that axis (or, if the eigenvalue is negative, that there is expansion along that axis). By diagonalizing the deformation tensor, the density near a particle can be re-written:

$$\rho = \frac{\bar{\rho}}{(1 - a\lambda_1)(1 - a\lambda_2)(1 - a\lambda_3)}, \quad (2.6)$$

where λ_i are the eigenvalues of the deformation tensor.

In the ZA, non-linearity occurs at a particle when $a\lambda_1 = 1$ ($\rho \rightarrow \infty$) which is equivalent to particles crossing the paths of other particles. Once this shell-crossing has occurred, the approximation has formally broken down, since there are no forces present to slow the particles and allow them to form clumps. The ZA as it was originally written is only valid for power spectra $P(k) \propto k^n$ where k is the wavenumber and $n \leq -3$ (Peebles 1980, 1993a,b). The reason for this strong restriction is that if $n > -3$ a substantial amount of power is allowed on small scales. As power is allowed on smaller scales, smaller objects form and the smaller the object, the earlier it forms. The earlier an object forms, the earlier it becomes non-linear, and therefore the earlier the ZA breaks down. A reasonably late-time realization of the ZA with such a power spectrum ($n > -3$) shows no readily recognizable structures.

An easy way to increase the range of spectral indices (as well as the length of time) for which the approximation is useful is to truncate the power spectrum (set $P(k) = 0$ for $k \leq k_*$) at a wavenumber (k_*) close to the one that is going nonlinear at the time of interest. This effectively removes the small scale modes and allows the effect of the larger ones to be seen. Granted, this means that the ZA is of no use whatsoever in predicting small-scale structures – they have been completely removed – however it *does* allow the large-scale structures to be seen correctly. As shall be seen in Chapter 4, the large modes apparently dominate

in determining the position of mass; small ones are effectively virialized and not correlated with their initial values.

2.2 The Truncated Zel'dovich Approximation

The truncated version of the ZA was first proposed by Kofman, et al. (1992) and is commonly called the Truncated Zel'dovich Approximation (TZA). It is accomplished by the same methods used for the untruncated version, save that the velocity potential is smoothed on a given scale before the velocities are calculated.

Coles, Melott, & Shandarin (1993) studied the quantitative agreement of several different approximate solutions with the “exact” N-body solution. They calculated the density cross-correlation coefficient:

$$S_{12} = \frac{\langle \delta_1 \delta_2 \rangle}{\sigma_1 \sigma_2} \quad (2.7)$$

where $\sigma_i \equiv \langle \delta_i^2 \rangle^{1/2}$. the subscript “1” refers to the N-body density field, and “2” refers to the density field of each approximation in turn. They found that a version of the TZA in which there was a sharp k -space cutoff at k_{nl} out-performed all other approximations tested over a range of spectral indices with one exception. The one exception was for the $n = -2$ case (the smallest spectral index they examined), in which the simple Zel'dovich Approximation performed the best.

Melott, Pellman, & Shandarin (1994) optimized the correlation of the TZA and corresponding N-body density fields by adjusting the form of the truncation and the wavenumber at which it is imposed. Their optimization was based on the cross-correlations of the density fields as defined above. I use their results:

$$P(k) \propto k^n e^{-k^2/2k_G^2}, \quad (2.8)$$

where n is the spectral index, k is the wavenumber, $k_G = ck_{nl}$ is the optimal Gaussian cutoff (c is indeterminably large for $n = -3$, so no cutoff is used; $c = 1.5$

for $n = -1$; $c = 1.0$ for $n = +1$; and $c = 0.8$ for $n = +3$). The non-linear wavenumber at the time of interest, k_{nl} , is defined by the equation:

$$a^2(t) \int_0^{k_{nl}} P(k) d^3k \equiv 1. \quad (2.9)$$

This truncation removes most of the strongly non-linear behavior and allows the familiar Zel'dovich pancakes to be seen. As shall be shown in Chapter 4, these pancakes are related to the real structures that form in N-body simulations.

2.3 References

- Coles P., Melott A. L., & Shandarin S. F. 1993, MNRAS, 260, 765
 Kofman L., Pogosyan D., Shandarin S. F., & Melott A. L. 1992, ApJ, 393, 437
 Melott A. L., Pellman T. F., & Shandarin S. F. 1994, MNRAS, 269, 626
 Peebles P. J. E. 1980. *The Large-Scale Structure of the Universe*. (Princeton: Princeton University Press)
 Peebles P. J. E. 1993a. in *Cosmic Velocity Fields*, eds Bouchet F. R. & Lachieze-Rey K.. (Gif sun Yvette. France: Editions Frontiers)
 Peebles P. J. E. 1993b, *Principles of Physical Cosmology*, (Princeton: Princeton University Press)
 Sahni V & Coles P. 1995. Physics Reports, 262, 1
 Zel'dovich Ya. B. 1970, Astronomy & Astrophysics, 5, 84

Chapter 3

The Shape of First Collapsed Objects

3.1 Introduction & Background

Since the early seventies, there has been a conjecture, based on the Zel'dovich approximation, that the first collapse of a self-gravitating dust-like medium results in the formation of a “pancake”-like object which is a thin surface. Recent work has cast doubt on this conjecture, suggesting instead that the first collapse may be pointlike or filamentlike instead of pancakelike.

The first analytical solutions for gravitational collapse considered very simple models, beginning with a spherically symmetric, pressure-free, non-rotating, monotonically decreasing over-density. In this instance, it was found that the over-density collapses to a point. If we allow the density perturbation, still spherical, to change *non-monotonically*, the collapse is to a shell. These cases are extremely simple and while they provide a decent approximation at a coarse resolution, they are a poor approximation to the real initial density fluctuations found in simula-

¹This chapter was based on research also published as Shandarin S. F., Melott A. L., McDavitt K., Pauls J. L., & Tinker J. 1995, Phys. Rev. Lett., 75, 7.

tions and expected in the early Universe. Also, one has only to glance at galaxy survey slices or N-body simulations to tell that mass does not generally appear in spherical concentrations. If a bit more non-uniformity is considered, such as the spheroidal over-densities studied by Lin, Mestel, & Shu (1965) the collapse is found to be to a spindle or disk, depending on whether the initial perturbation was prolate or oblate. Then in 1970, Zel'dovich formulated an approximate solution to the problem of gravitational collapse of a collisionless medium (see Chapter 2). This approximation defined, for each point, three eigenvectors and predicted that a generic collapse would proceed at different rates along each of these three axes, resulting in a thin surface whose normal is the axis of fastest collapse. This solution is analytic within the approximation, and has been accepted by some as the correct way of viewing the dynamics and shape of the first collapse, even outside the approximation.

More recently, some doubt has been cast on whether this collapse to thin sheets is generically correct. Gurevich & Zybin (1988) considered a nondissipative gravitational collapse of a generic perturbation and concluded that it forms a stationary dynamical structure with a pointlike singularity at its core with $\rho \propto r^{-24/13}$. Further, Bertschinger (1993) and Bertschinger & Jain (1994) suggested a purely local solution to gravitational instability that resulted in a generic first collapse to filaments. This approximation was later shown (Kofman & Pogosyan, 1995; Bertschinger & Hamilton, 1994) to be faulty. It drew conclusions about structures formed in the Newtonian limit from a theory that had neglected terms which, while insignificant in the ultra-relativistic limit, were important in the Newtonian limit. The difference in collapse scenario between these two limits was stressed by Zel'dovich & Novikov (1983). One can, of course, also raise a question about whether the claim from the Zel'dovich approximation that the generic first collapse is to sheets can be correctly applied to non-linear gravitational clustering. It is known, for example, that collapse in N-body simulations proceeds faster than

the Zel'dovich approximation predicts. So the question of the shape of the first collapsed objects is still open to examination.

In this chapter, the first objects to collapse in several N-body simulations are studied in an attempt to settle this question.

3.2 The Simulations

The following discussion is based on an ensemble of five N-body simulations with initial power spectra $P(k) \propto k^{-1}$ which were created with a sufficiently low initial amplitude ($\delta_{rms} \sim 0.03 - 0.04$) that they are indistinguishable from Eulerian linear perturbation theory. This low amplitude also allows enough evolution time (an expansion factor of about 17) for transients to die out and the full growing mode with nonlinear effects to establish itself (Scoccimarro, 1997). As a check, two models (3 and 4 in Table 3.1) were started with half the initial amplitude and run for twice the expansion factor. They show no noticeable differences. The initial fluctuations were constructed to correspond to wavenumbers between 1 and $\sqrt{3}$ in units of the fundamental frequency, making the minimum wavelength present 74 mesh units, for four of the simulations. The upper, $\sqrt{3}$, limit is the smallest upper limit possible without causing the structure to be artificially aligned with the coordinate axes. The fifth simulation (simulation 5 in Table 3.1) allowed wavenumbers from 1 to 3 as a check. The first object to collapse was a bit smaller than in the other cases, which is natural since smaller waves were permitted, but its shape and relative dimensions were consistent with the other simulations.

The time-steps were very strictly constrained, allowing the fastest particle to go no further than 0.4 cells in a single time-step. The simulations were stopped after the *first* time-step in which there was a particle that had undergone shell-crossing. Shell-crossing is defined as the point at which a particle is associated with a negative volume element ($\mathbf{x} \otimes \mathbf{y} \cdot \mathbf{z} < 0$). This can be physically interpreted as a volume element collapsing “through” itself. In the Zel'dovich approximation this is

Table 3.1: Information on the first collapsed objects in the simulations

Simulation	Thickness (mesh units)	Width (mesh units)	Length (mesh units)
1	0.8	17	37
2	0.6	32	37
3	0.5	5	16
4	0.8	7.5	48
5	0.1	3.5	8

equivalent to the particle crossing the trajectory of another particle and entering a multi-stream region. This is how the Zel'dovich approximation defines a collapsed object and while it does not guarantee that our object is gravitationally bound (strictly speaking, nothing becomes gravitationally bound in the approximation), it is likely that it will become so. Further, it provides a good, clean definition of the particles with which we want to deal. It is worth noting here that at the very first time-step at which there is shell-crossing, thousands of particles typically cross. The first collapsed object is therefore defined as the one formed by the set of all particles that underwent shell-crossing in that first step. The distribution of such particles was examined for the five simulations. For consistency figures are presented from only one simulation; the others are qualitatively similar.

Figures 3.1, 3.2, and 3.3 show three views of the first collapsed object in simulation 1 in Table 3.1. The views are projections along the three eigenvectors of the initial deformation tensor (from the Zel'dovich approximation) towards the center of the collapsed object. Figures 3.1 and 3.2 suggest that the object has a substantial thickness of about 4 cells. However, if the object is considered in cross-sectional slices (2 grid cells thick, instead of the effective 17 or 37 grid cells in Figures 3.1 and 3.2, respectively) as in Figures 3.4 and 3.5, it can be seen that the object is in fact quite thin. Looking at several of these slices in succession (not reproduced here), we can tell that the shape is bowl-like; hence the projections of the whole object in Figures 3.1 and 3.2 seem to be thick. The *true* thickness of the shape, obtained from measurements of its thickness in the thin cross-sectional

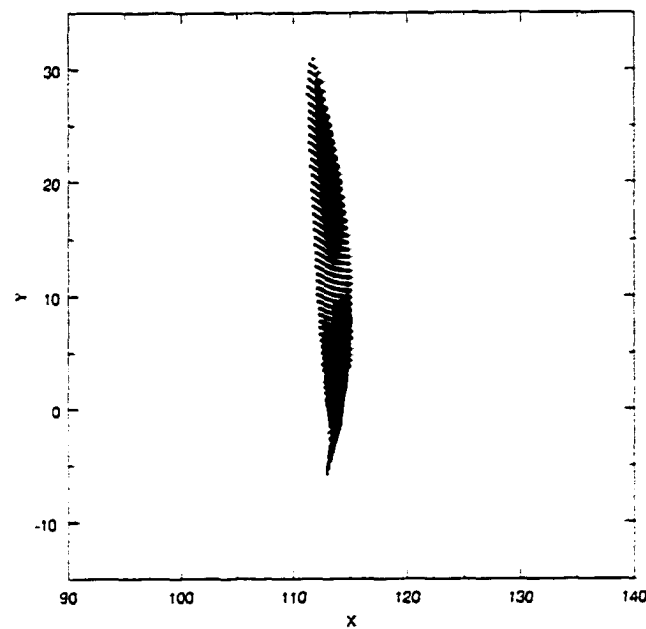


Figure 3.1: Projection of all the collapsed points from Simulation 1 into the xy-plane after the first time-step in which shell-crossing had occurred.

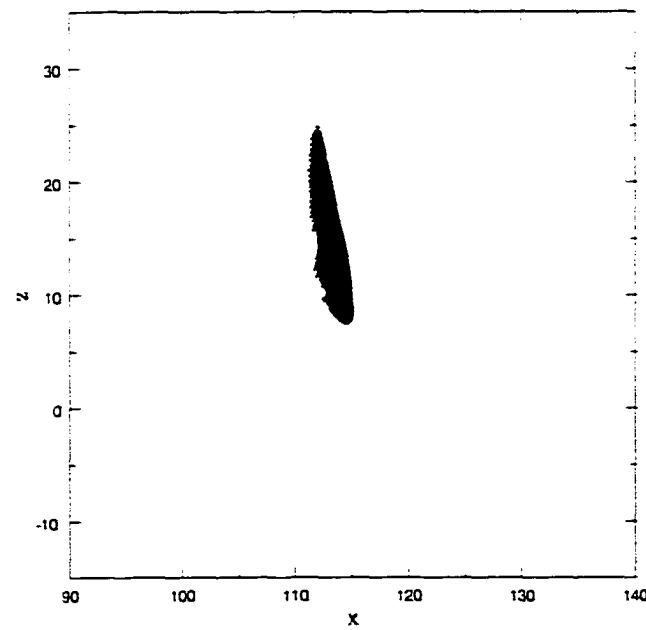


Figure 3.2: As in Fig. 3.1, projection into xz-plane.

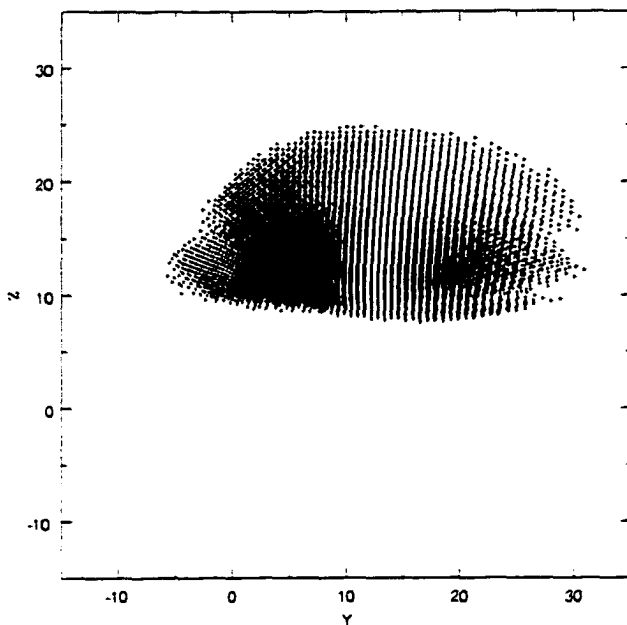


Figure 3.3: As in Fig. 3.1, projection into yz -plane.

slices. is just under one cell. The ratios of the dimensions of the first collapsed object are found to be 1:17:37 – describing an extremely shallow, oval bowl-like object. This is categorized as collapse to a sheet. The object formed in simulation 4 could perhaps best be described as a ribbon, but note that even in that case, the smallest dimension is still nearly *ten times* smaller than the next largest – leading to its categorization as a sheet-like object as well. In fact, the objects in all five of the simulations were best fit in the category of sheet-like.

At this point it is prudent to make two comments relating to the appearance of these figures. First, the particles seem to follow a sort of distorted grid. This is the nature of simulations which begin with small initial perturbations from a cubic lattice (and little or no small-scale power) and is a reflection of the smooth initial fluid-like flow of the particles. It should not be cause for concern. At later stages, as the simulation becomes nonlinear, the grid will disappear.

Second, since the particles plotted in Figures 3.1- 3.5 are only the ones which

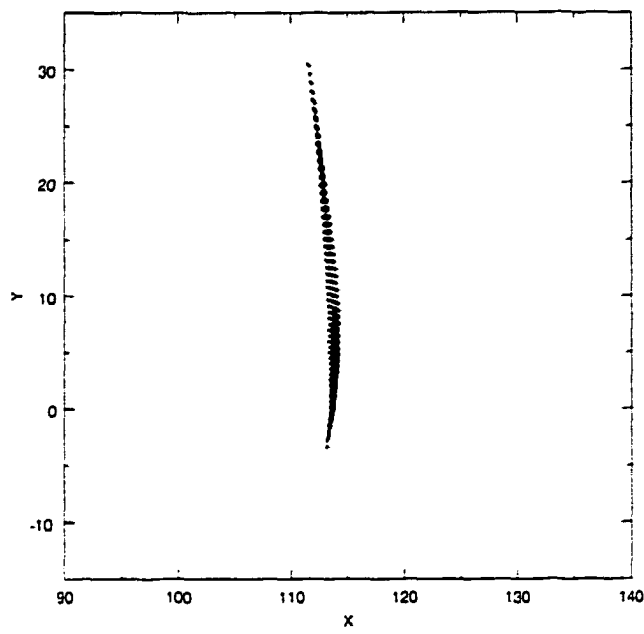


Figure 3.4: A thin slice (2 mesh units) through the center of the pancake as shown in its orientation in Figure 3.1.

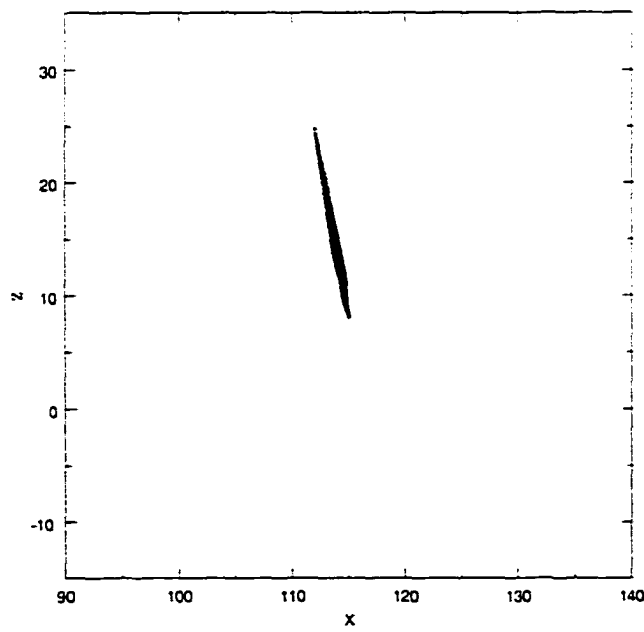


Figure 3.5: A thin slice (2 mesh units) through the center of the pancake as shown in its orientation in Figure 3.2.

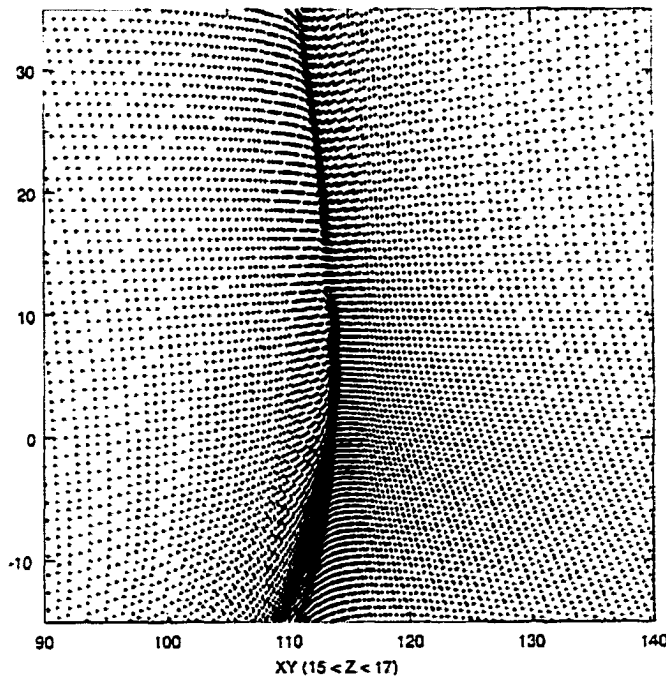


Figure 3.6: A thin slice (2 mesh units) through the center of the pancake as shown in its orientation in Figure 3.1, but containing all points.

have gone through shell-crossing, they do *not* necessarily give a fair representation of the overall density in the simulation. To investigate that idea further, Figures 3.6, 3.7, and 3.8 are included which show *all* particles in thin slices centered on the object. These slices have the same thicknesses as, and should be compared to, Figures 3.4 and 3.5, (and not to Figures 3.1, 3.2, and 3.3). It appears that the region of highest density is larger than the collapsed object. This is not surprising, as thousands more particles are on the verge of shell-crossing and would be included in the object in the next time step, if it was taken. The important thing to note is that if a visual assessment of the shape of the highest density region is made, roughly the same relative dimensions will be found for it as were found for formally-defined collapsed object.

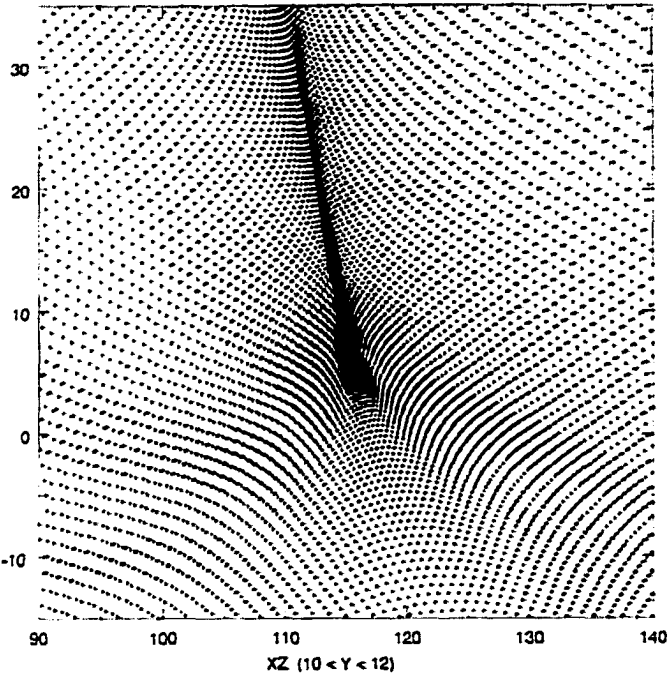


Figure 3.7: A thin slice (2 mesh units) through the center of the pancake as shown in its orientation in Figure 3.2, but containing all points.

3.3 Conclusions

These five simulations suggest that the first collapse from generic perturbations in a gravitating medium is usually to a sheet, as suggested by the Zel'dovich approximation. While this result is applicable to all scales, from stars to superclusters, it seems that the primary scale of interest today will be superclusters, since they represent the scale that is undergoing its first collapse at the present.

When observations such as galaxy survey slices are considered, it may seem that filaments are extremely prevalent, perhaps more so than sheets. As well, looking beyond the Zel'dovich approximation, it can be found in second-order perturbation theory that the rate of collapse along one axis can affect the rates of collapse along the other axes, possibly changing the shape of the collapsed object. In response to that, it should be pointed out that filaments may be easier to see than sheets due to their higher density contrast and possibly gas cooling effects

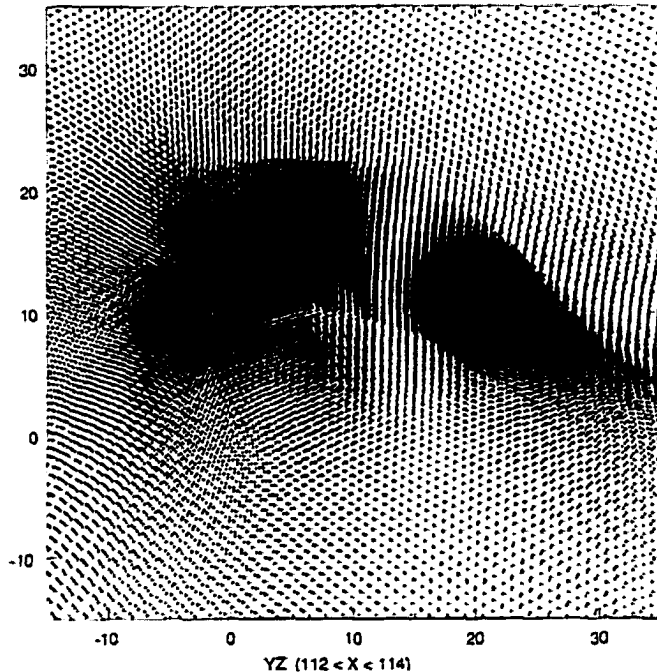


Figure 3.8: A thin slice (2 mesh units) through the center of the pancake as shown in its orientation in Figure 3.3, but containing all points.

(Ostriker, 1995). This indicates that they may not be the dominant shape. Also, filaments can be formed within the framework found in this study, most commonly as second generation structures, formed as matter further collapses within sheets (and perhaps occasionally as first collapse objects). Also, returning to theory, the general solution with the maximal number (eight) of physically arbitrary functions of three variables suggests gravitational collapse is to sheets (Lifshitz, et al. 1961, and Grishchuk 1967). Observationally, there is some very recent, exciting evidence for sheet-like objects composed of neutral hydrogen at moderate redshifts (see, for example, Dinshaw, et al., 1995, and Crotts, 1997). This idea will resurface in Chapter 6. So while it may seem at first that observations are dominated by filaments, there are reasonable explanations for this appearance and it does not discount the conclusions of this work.

If the simulations are generalized to include small-scale perturbations, the first objects formed are not expected to be as smooth as those presented here. The

first objects to collapse (from the smallest-scale perturbations present) will not be as smooth due to resolution limitations; larger objects, at the time they become non-linear, will be later generation objects and therefore not as smooth due to the smaller-scale perturbations present. However, the general dimensional ratios are not expected to change substantially.

Let's look at the significance of these results. If we make the prior hypothesis that first collapse to sheets is equally as likely as first collapse to all other shapes (points or filaments), then this outcome (five sheets in five simulations) should occur only 3% of the time and the hypothesis can be rejected with 97% confidence. Alternatively, we can try to estimate the likelihood with which sheets occur, given this outcome. If we assume that our outcome is more likely than all others (that is, will occur at least 50% of the time), the probability that first collapse is to sheets must be at least 87%. While these results point strongly towards first collapse *usually* being to sheet-like objects, they certainly do not rule out occasional first collapse to other shapes. So we see that there are many competing ideas, but when we examine our simulations, which are not based on any of the approximations discussed (except for setting the initial conditions at very low amplitude), are allowed to gravitationally evolve for many expansion factors, and for which we have complete (to resolution limits) information about the mass distribution, we find that *in general, mass collapses under gravity to form sheets*.

3.4 References

- Bertschinger E. 1993, *Cosmic Velocity Fields*, eds Bouchet F.R. & Lachieze-Rey M., (Editions Frontiers, Gif sun Yvette, France), 137
- Bertschinger E. & Hamilton A. 1994, ApJ, 435
- Bertschinger E. & Jain B. 1994, ApJ, 431

- Crotts A. P. S. 1997, to appear in *Proceedings of 13th IAP Colloquium: Structure and Evolution of the IGM from QSO Absorption Line Systems*, eds. Petitjean P. & Charlot S.
- Dinshaw N., Foltz C. B., Impey C. D., Weymann R. J., & Morris S. L., 1995
Nature, 373, 223
- Grishchuk L. P. 1967, Sov. Phys. JETP, 24, 320
- Gurevich A. A. & Zybin K.P. 1988, Sov. Phys. JEPT, 67, 1
- Kofman L. A. & Pogosyan D. 1995, ApJ, 442, 30
- Lifshitz E. M.. Sudakov V. V., & Khalatnikov I. M. 1961, Sov. Phys. JETP, 13, 1298
- Lin C. C.. Mestel L., & Shu F. M. 1965, ApJ, 142, 1431
- Ostriker J. P. 1995. personal communication
- Scoccimarro R.. 1997 preprint, astro-ph/9711187 at <http://xxx.lanl.gov/archive/>
- Zel'dovich Ya. B. 1970. A&A. 5, 84
- Zel'dovich Ya. B. & Novikov I. D. 1993. *The Structure and Evolution of the Universe*. (University of Chicago. Chicago), Chap. 19

Chapter 4

Hierarchical Pancaking

4.1 Introduction

The Zel'dovich approximation, discussed in Chapter 2, provides one approximate solution to the problem of gravitational clustering. This solution is characterized by large “pancake”-like structures. In this model, structures form from the “top-down” – that is large-scale objects (several ten’s of Mpc) form first, then smaller objects (clusters of galaxies down to galaxies) form in the rich over-dense regions of the pancakes. This is in direct contrast to the “bottom-up” or *hierarchical* model of structure formation in which smaller objects are the first to form and then they gravitationally interact on larger and larger scales to form clusters and super-clusters of galaxies.

Neither model can yet claim to completely describe the rich variety of voids, sheets, filaments, and clusters that seem to populate the Universe. In this chapter I will look at individual structures and attempt to explain them as the convergence of these two classic, but seemingly contradictory, models.

If one looks at two slices – one through an N-body simulation and one through the Zel'dovich approximate solution of the same initial conditions (figure 4.1)

¹This chapter was taken largely from Pauls J. L. & Melott A. L., 1995, MNRAS, 274, 99.

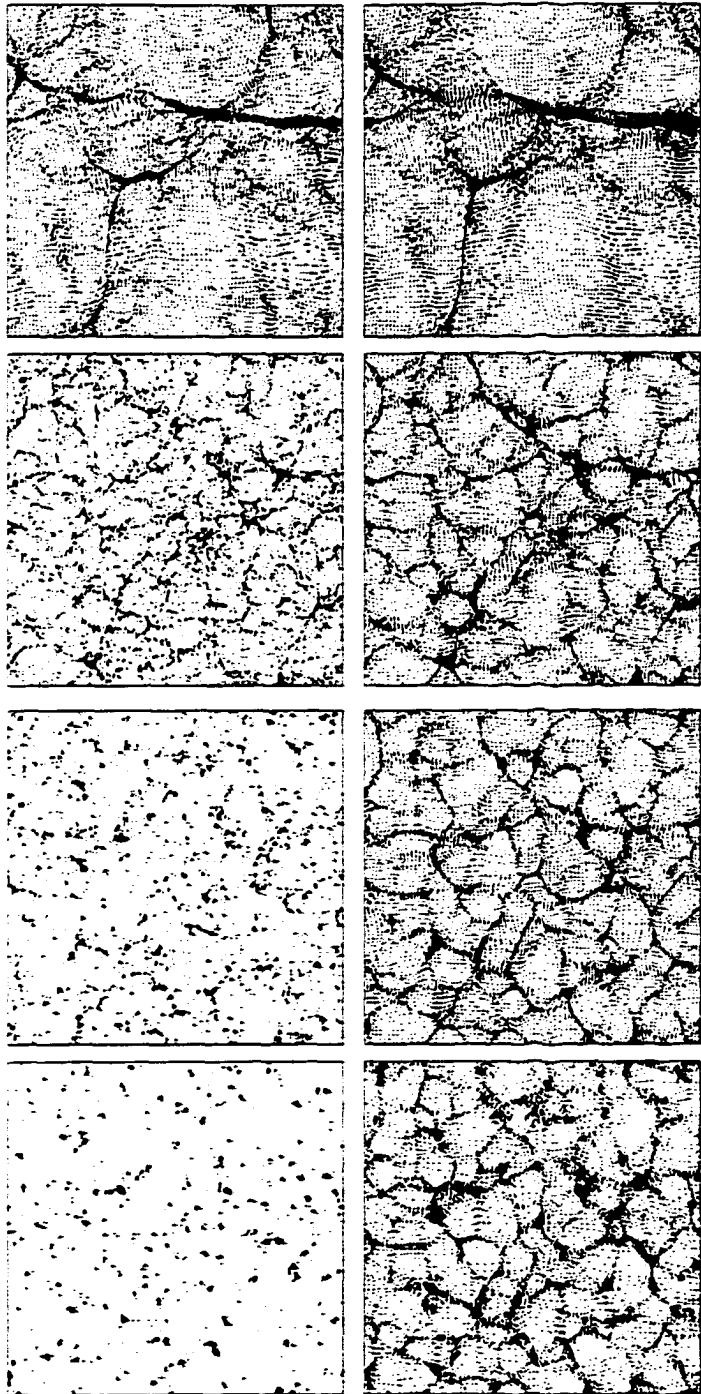


Figure 4.1: Thin slices taken from N-Body (left) and TZA (right) realizations with the same (random) phases with various spectral indices. The moment shown is $k_{nl} = 8k_f$: where k_f is the fundamental mode of the box. Top row: $n = -3$; second row: $n = -1$; third row: $n = +1$; bottom row: $n = +3$.

– it is not hard to imagine that the “pancakes” characteristic of the Zel’dovich Approximation also appear, in roughly the same places, in hierarchical N-body simulations. (To see that the shapes are truly sheets, it is necessary to look at a number of adjacent slices and observe how the structures that look filamentary in 2D are, in fact, cross-sections of large, thin sheets.)

Coles, Melott, & Shandarin (1993) verified this to some extent when they compared the density fields. Looking into the question more deeply, I found that the orientation and position of individual objects in N-body simulations can be predicted rather well using the TZA – that is, Zel’dovich pancakes are present in N-body simulations. The agreement (as with the density fields) is best for $n = -3, -1$ and the accuracy decreases for increasing large- k power in the initial conditions. Even in the most extreme (traditionally hierarchical) case examined, with initial power spectrum $P(k) \propto k^3$, it was found that the TZA worked reasonably well. This implies that even very low-amplitude long waves will dominate and control the overall motion of the smaller clumps which form earlier by the collapse of shorter wave perturbations. In this case ($n = +3$) the correlation length of the initial potential is extremely small. It is explicitly verified that the coherence length of the potential grows substantially for power laws $n \geq +1$, explaining the coherent movement of clumps into second-generation pancakes. It is shown that the nonlinear (evolved) gravitational potential strongly resembles the smoothed initial potential. This explains why ZA with smoothed initial conditions reproduces large-scale structure so well, and probably why our Universe has a coherent large-scale structure.

This study considered the superpancakes (Kofman et al. 1992) which form in N-body simulations with spectral indices $n = -3, -1, +1, +3$ evolved to $k_{nl} = Sk_f$. Such models yield a final effective box size of $168h^{-1}Mpc$ and particle mass (assuming $\Omega = 1$) of $6.3 * 10^{11}h^{-1}M_\odot$ for the $n = -1$ case and a $140h^{-1}Mpc$ box and $3.6 * 10^{11}h^{-1}M_\odot$ particle mass for the $n = +1$ case, based on scaling from the

correlation length as described by Melott & Shandarin (1993). In Figure 4.1b it is seen that the structure apparent in a slice through a simulation with $n = -1$ is similar to that found in the Las Campanas Survey (Figure 1.1) and that this structure is understandable in terms of Zel'dovich pancakes. For the purpose of this discussion, sheets and filaments, which both form in simulations (Babul & Starkman 1992) and in the TZA will not be distinguished.

4.2 Comparison of the TZA with N-Body “Superpancakes”

When comparing a slice through an N-body simulation to a slice through the TZA realization of the same initial conditions, one can immediately see that large structures form in the same places and have roughly the same orientations (see Figure 4.1). The structures in the N-body case are known as second-generation pancakes (Peebles 1993a) or superpancakes because in the N-body case, power is allowed on all resolved scales and small objects have already become non-linear. The larger structures are a later “generation” of structures to go through collapse.

In the TZA, structure is formed (to first order) by spheres deforming into ellipsoids. So to do a comparison to N-body models, a method to select spheres in the initial conditions that will be characteristic of the N-body filaments is needed. So the first task is to choose appropriate centers and radii for the spheres. Two related methods suggest themselves. One approach is to pick a point at the center of a perceived filament and build a sphere around it. Specifically, the filament is approximated as a thin cylinder and the particle nearest the center of mass of the filament in its initial (Lagrangian) coordinates is chosen. Or instead one could choose the center by looking for a peak in the TZA eigenvalue field that is close to the (initial) center of mass of the filament. These peaks are “birth points” for pancakes – a natural starting point from the point of view of the TZA.

Presumably these two methods will yield points separated by only one or two grid cells, and those differences could be attributed to small errors in visually choosing the filament. Both methods were tried and it was found that while the two points *usually* are quite close and move towards each other as the model evolves, they do not always do so. Sometimes the TZA peak seems to be associated with a rather large clump (one of several in the filament), rather than with the filament as a whole, and the centers of mass move apart. Therefore it is unwise to blindly characterize the filaments by their nearest eigenvalue field peak (although in most cases such a characterization is accurate), and the spheres were instead chosen using the Lagrangian center of mass process.

It should be noted that this procedure (selecting filaments rather than sheets) has introduced a bias towards objects with two axes collapsing near the same time. This choice has no special meaning beyond the fact that filaments have a higher density contrast and are therefore easier to see. The general verbal usage will be followed and references to "pancaking" should be assumed to mean the formation of anisotropic structures. Whether they are prolate or oblate depends on the ratios of eigenvalues and the stage of evolution (e.g. see Babul & Starkman 1992).

The procedure is fairly simple. A (straight) filament is visually selected and approximated as a cylinder. Then the particle nearest the Lagrangian center of mass of those particles which will end up in the filament is found. The particles in a sphere around the center of mass are tagged, making sure that the radius is large enough to fairly approximate a sphere but not so large that it includes particles from outside the filament – an average sphere will contain on order of 100-200 particles. These particles are then followed through their N-body evolution and their deformation is compared to the deformation predicted by the TZA. This is illustrated in Figures 4.2, 4.3, 4.4, 4.5, for the various spectral indices. It can be seen that pancaking occurs in each of these figures. The difference lies in

the relative sizes of the components making up the pancakes, not in their overall shapes. I conclude that the generic pancake form occurs for each of these spectral indices.

Statistics are built for the N-body distribution by computing the tensor (van Haarlem & van de Weygaert 1994):

$$I_{ij} = \frac{1}{n} \sum_{k=1}^n (x_{ik} - \bar{x}_i)(x_{jk} - \bar{x}_j) \quad (4.1)$$

k is clearly summed over the number of particles, while i, j each run from 1 to 3 for the dimensionality of the ellipsoid. Therefore " x_{ik} " represents the i th component of the k th particle. This tensor has the same eigenvectors as the inertia tensor:

$$\text{inertia tensor}_{ij} = \frac{1}{n} \sum_{k=1}^n \delta_{ij} x_k^2 - I_{ij} \quad (4.2)$$

where $x_k^2 = (x_{1k} - \bar{x}_1)^2 + (x_{2k} - \bar{x}_2)^2 + (x_{3k} - \bar{x}_3)^2$, but its eigenvalues are the mean squared displacements of the points from each plane defined by a pair of principal axes. These principal axes are compared with the eigenvectors of the TZA deformation tensor calculated for the particle at the center of the Lagrangian sphere. This tests whether the TZA is doing a good job of predicting the filament orientation. The ratios of the square roots of the eigenvalues from I are calculated to give flattening data. For a uniform ellipsoid, it can be shown that these ratios are equivalent to the ratios of the lengths of the corresponding semi-axes. To simplify the calculation, the center of the ellipsoid is positioned at the origin and the semi-axes are aligned along the coordinate axes (that is, the principal-axis transformation is done). Then the off-diagonal elements vanish (for each $(xy)dxdydz$ element there is an $(xy)dxdy(-dz)$ element, etc.) and the diagonal elements become $I_{ii} = \frac{1}{n} \sum_{k=1}^n x_{ii}^2$. If the lengths of the semi-axes are a, b, c , corresponding to x, y, z respectively, then for an ellipsoid of uniform density, this sum becomes the integral (for $x_{11} = x$):

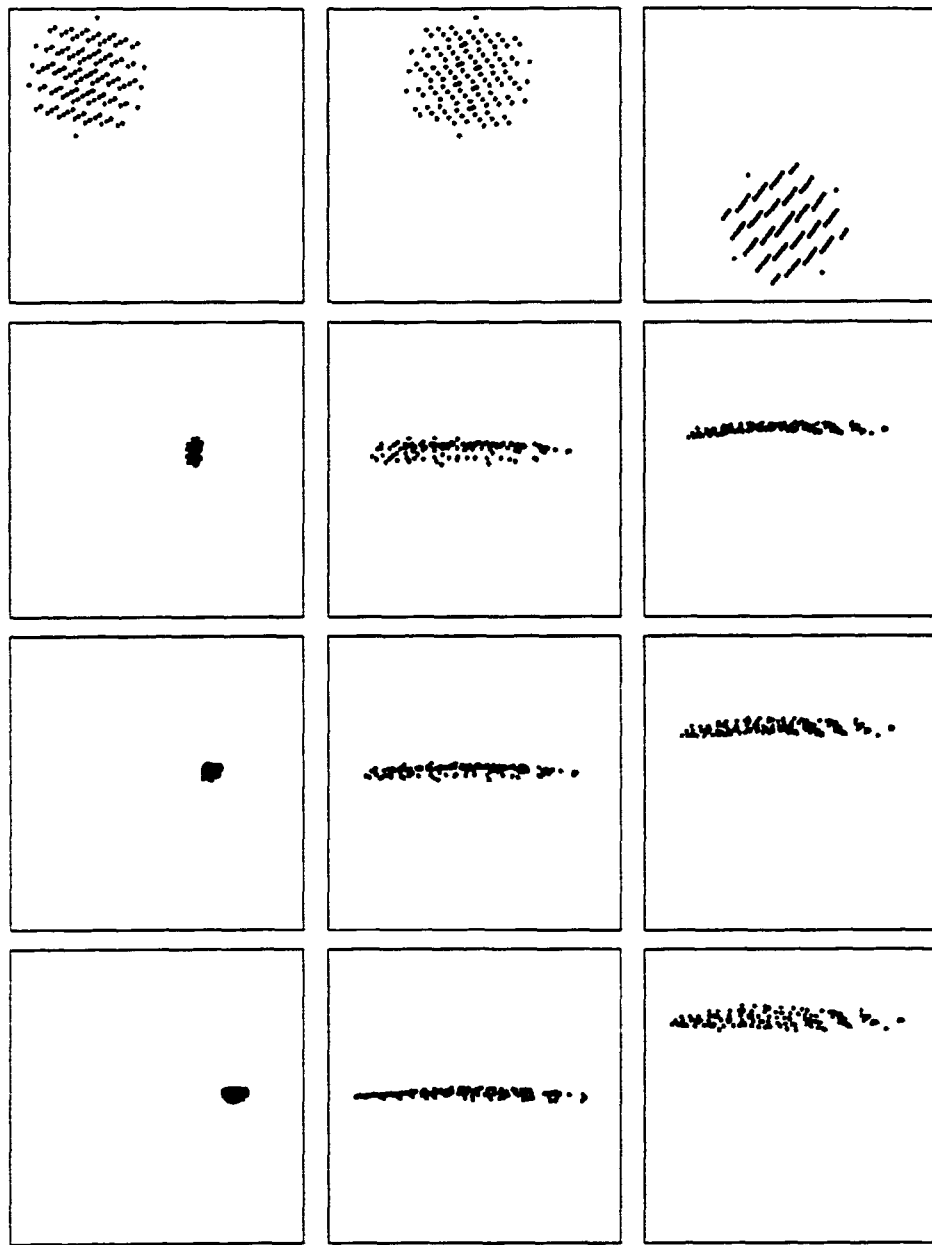


Figure 4.2: Projections of the particles initially in a sphere chosen by the method detailed in Section 4.2. The three columns show the projections along the three eigenvectors calculated using Equation 4.1. The four rows show these projections at four stages: initial positions, $k_{nl} = 32k_f$, $k_{nl} = 16k_f$, and $k_{nl} = 8k_f$; where k_f is the fundamental mode of the box. The filaments were selected when $k_{nl} = 8k_f$. The initial spectral index is $n = -3$.

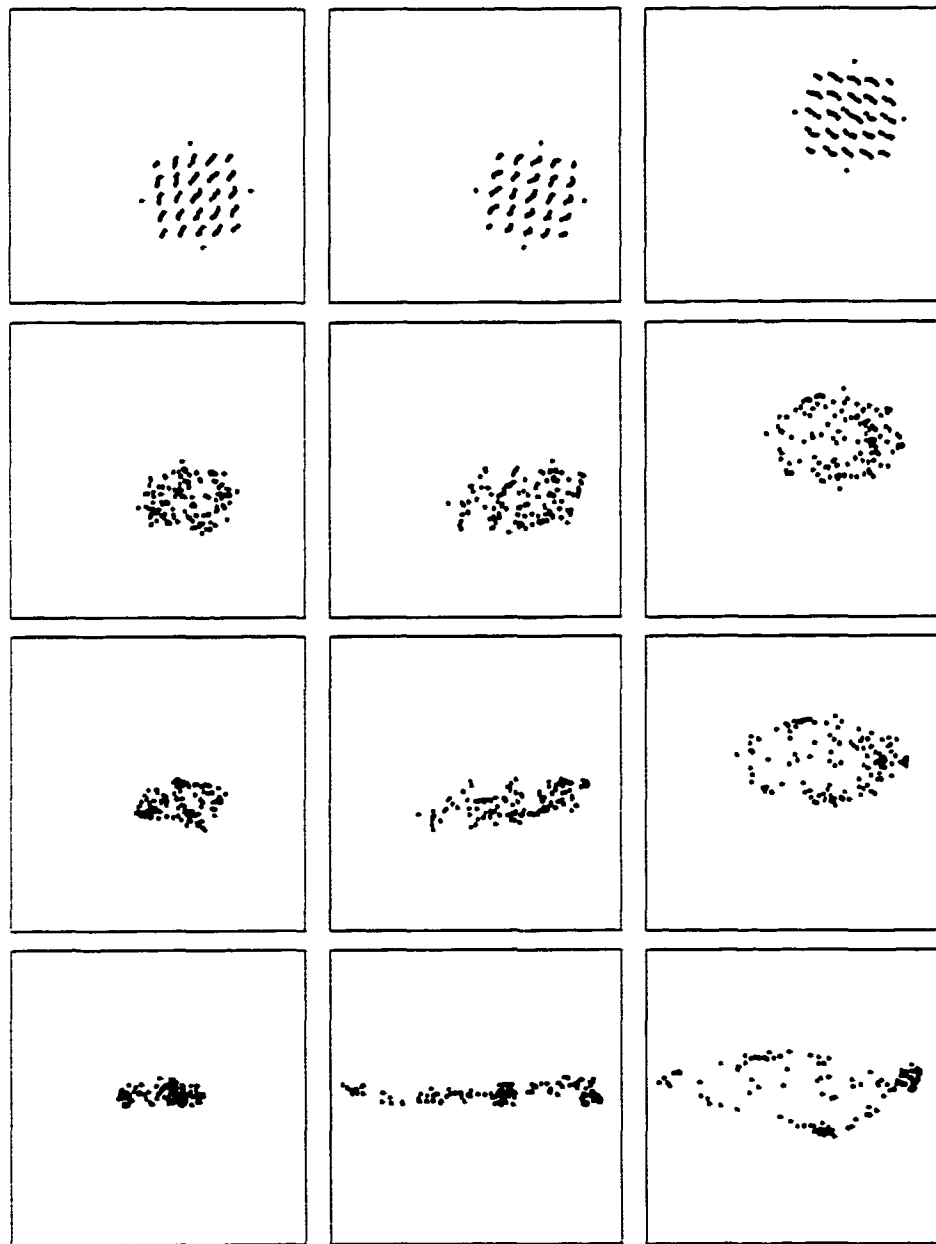


Figure 4.3: As Figure 4.2, with $n = -1$.

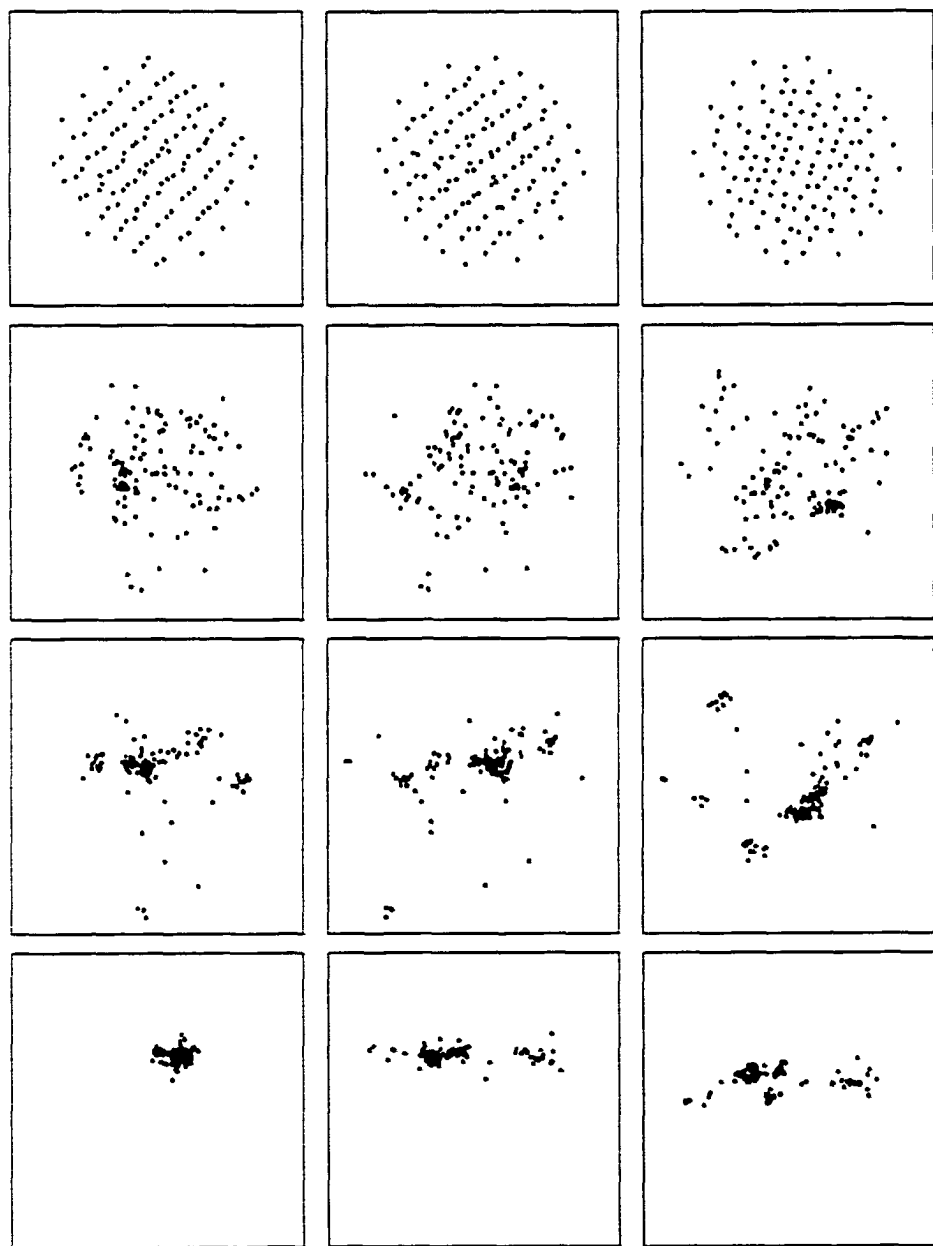


Figure 4.4: As Figure 4.2, with $n = +1$.

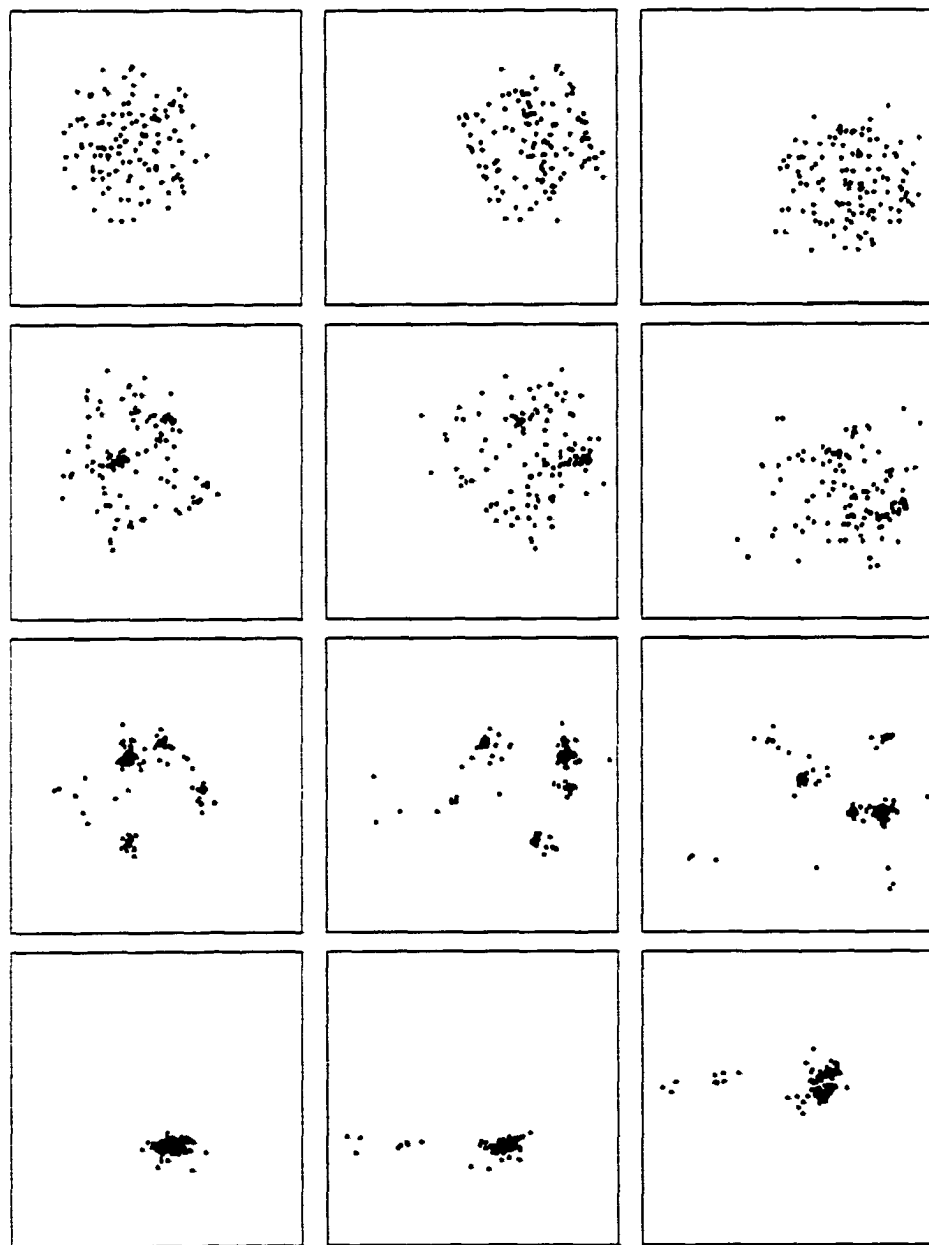


Figure 4.5: As Figure 4.2, with $n = +3$.

$$I_{11} = \frac{1}{V} \int x^2 dV = \frac{2}{V} \int_0^a \int_0^b \int_0^c \sqrt{1 - \frac{x^2}{a^2} - \frac{y^2}{b^2}} x^2 dx dy dz. \quad (4.3)$$

Doing the integrals, we get:

$$I_{11} = \frac{2cb\pi}{V} \int_0^a x^2 \left(1 - \frac{x^2}{a^2}\right) dx = \left(\frac{4\pi abc/3}{V}\right) \frac{a^2}{5} = \frac{a^2}{5}. \quad (4.4)$$

Similarly:

$$I_{22} = \frac{b^2}{5} \quad \text{and} \quad I_{33} = \frac{c^2}{5}. \quad (4.5)$$

Now it is clear that the ratios of the square roots of the eigen-values are equal to the ratios of the lengths of the semi-axes.

The results of the comparisons are remarkably good. Each I eigenvector was matched with the Zel'dovich eigenvector along the direction which it most nearly points. The average angular difference between all these pairs was found to be $(14 \pm 13)^\circ$ for the $n = -3$ case. $(13 \pm 9)^\circ$ for the $n = -1$ case. $(17 \pm 10)^\circ$ for the $n = +1$ case, and $(26 \pm 12)^\circ$ for the $n = +3$ case. We might expect better agreement if we consider only the axes which point along the most characteristic dimension (either the longest, for a more filamentary structure, or the shortest, for a more oblate structure) were considered. That is, the two axes perpendicular to the characteristic dimension of the structure could be more difficult for I to distinguish, while the TZA has them "built in". (In the worst case scenario, imagine an ellipse with a, b, c as its semi-axes. If $b=c$, then the principal axes associated with b and c have completely arbitrary orientations in a plane.) However, comparisons of only these pairs yield improved agreement only in the $n = -3$ case where there is nearly a factor of 2 improvement in the angular agreement.

Finally the axis pairings the eigenvalues predicted were examined. The TZA had formally broken down for more than half of the structures examined and might be thought to be of no use in predicting these pairings. However, since the

TZA eigenvalues give the relative time of collapse, their *order* ought to still be correct. Although the TZA pancakes are becoming “puffy” after shell-crossing has occurred, their N-body counterparts are still collapsing. It is therefore reasonable to expect that the direction that the TZA gives as the earliest to collapse may be the same as the most completely collapsed direction in the N-body case at any time, even after the TZA pancake has shell-crossed. The largest compression from the TZA is therefore matched with the shortest semi-axis of I . In the $n = -3$ case, these pairings were the same as the minimal angle pairings 95% of the time, with the remaining 5% clearly falling prey to the problem of the two smaller eigenvalues being nearly identical. In the $n = -1$ case, these pairings were *always* the same as the minimal angle pairings. In the $n = +1$ case, the pairings were the same nearly 90% of the time. And even in the $n = +3$ case, the pairings were the same 70% of the time. One would expect only 1 in 6 (17%) of the pairings to be correct if we compared two randomly oriented sets of coordinate axes that had randomly assigned eigenvalue order.

Peebles (1993a) has suggested examining axial ratios inside a collapsed Lagrangian sphere as an objective test for identifying a model containing “super-pancakes”. His suggested criteria (personal communication) was a 2:1 (or better) flattening of spheres for an $n = -1$ model.

The maximal flattening ratio (that is, the ratio of the longest to shortest axes for each of the chosen filaments/pancakes) was found to be 10.0 ± 4.9 ; the ratio of the middle to the shortest axis is 3.0 ± 2.8 for $n = -3$. For $n = -1$, the maximal flattening ratio was 5.4 ± 2.4 and the middle ratio is 2.4 ± 0.7 . For $n = +1$, the maximal flattening is 7.0 ± 3.2 and the middle ratio is 2.3 ± 0.9 . For $n = +3$, the maximal flattening is 6.7 ± 3.5 and the middle ratio is 2.5 ± 1.2 . These axial ratios (also shown graphically in Figure 4.6) are remarkably similar across a wide range of spectral indices, further substantiating the claim that pancake structures form even in models with substantial small-scale power. Since shell-crossing has

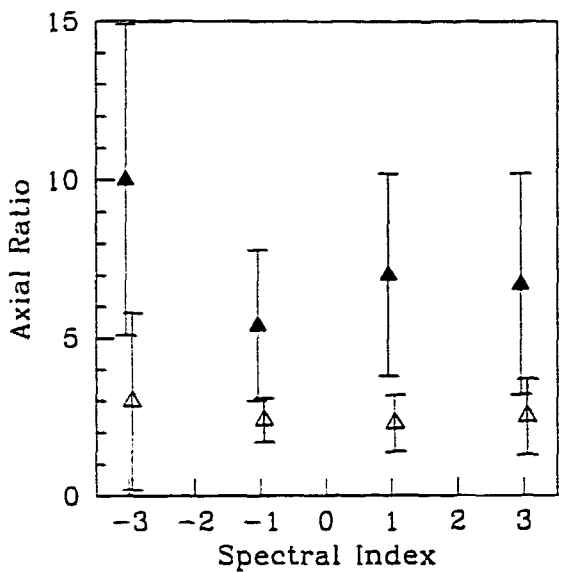


Figure 4.6: The ratios of longest:shortest (filled triangles) and middle:shortest (open triangles) axes for several models.

already occurred, or is extremely close to occurring in almost all filaments. the TZA cannot be used to make a numerical prediction of these ratios.

An additional check of the general plausibility of the TZA was done by looking at the amount of mass in nonlinear objects in the N-body simulation versus the TZA. The N-body slices appear to have more particles (mass) in clumps than do the TZA slices (Figure 4.1). For $n = -1$, which is probably closest to the slope on the scales of objects going non-linear today, the total number of particles which have shell-crossed in the TZA was compared to the total number of particles in the simulation which ever had a negative volume element ($a \times b \cdot c$, where a , b , and c are the vectors from a point to the current positions of its Lagrangian neighbors along each box axis). It was found that 36% of the TZA particles were clumped, compared to 50% of the N-body particles. This is considered to be reasonable agreement.

It has been shown that quasilinear structure in hierarchical N-body models can

be approximated very simply as gravitational amplification of initial anisotropies during collapse. This was achieved by showing that when the ZA is truncated using the method of Melott, Pellman, & Shandarin (1994), it can accurately predict where moderately nonlinear structures (like clusters and superclusters) will form, their orientations, and their relative prolateness or oblateness. It can further be concluded that no exotic theories are required to describe such structure formation. Gravitational amplification of Gaussian perturbations is entirely adequate. Up to this point, I have been concerned with the question of how well the TZA works. Next let me turn my attention to the more interesting question of *why* it works.

4.3 Why Do Super-Pancakes Exist?

Recent years have seen numerous numerical tests that demonstrate the similarity between the locations of clumps in hierarchical clustering models and the tracing of pancakes found by applying the ZA to the smoothed initial conditions (MPS. and references therein).

Another approximation to gravitational instability, the approximate theory of adhesion (Gurbatov, Saichev, & Shandarin 1989; Kofman et. al. 1992), offers one explanation. This approximation suggests that mass will move in a smooth flow up to R_* , roughly the peak-to-peak length scale associated with the initial potential, providing pancakes. After this, the clumps formed move coherently in response to the potential, producing “second-generation pancakes” or “superpancakes”. This stage is supposed to last until the clustering reaches the scale of the correlation length of the initial potential, R_ϕ . Then there is the third regime in which the filaments predicted by the adhesion approximation correspond to at best a clump or two and therefore can’t be identified as filaments at all. This regime is pure hierarchical clustering, in which motions are dominated by local clumps and the initial potential is irrelevant. (This last stage was traditionally assumed to be

the only one in hierarchical clustering theory, which never predicted filamentary structure.)

The first stage is relevant only for initial fluctuation spectra which drop off sufficiently rapidly at large k , or have a forced cutoff as in numerical simulations. The second stage describes the models $n = -3, -1$ as far as they are evolved for this study. The third stage supposedly describes the models $n = +1, +3$. Evidence will be presented that the third stage does not exist, at least for $n \leq +3$. There seems to be no particular change in behavior at R_ϕ , and a severe test of the relevance of the correlation length in the initial potential has been designed. An N-body simulation with an initial spectral index $n = +3$ has been run. In this extreme case the correlation length of the initial potential R_ϕ is extremely small, resolution limited (the actual calculation puts the correlation length at less than a cell). According to previous discussions of adhesion, there should be essentially no similarity between the N-body simulations and any motions resulting from the initial potential at any stage expected. In Figure 4.1, dot plots of thin slices of the N-body simulation and of the TZA are shown. (Incidentally, the optimal Gaussian truncation length for $n = +3$ was determined to be $k_G = 0.9k_{nl}$, using the method of MPS.) The moment shown is $k_{nl} = 8k_f$. While the approximation is not precise, it is nevertheless obvious that there is a strong tendency for the positions of condensations to agree. It is useful to examine the density correlation coefficient,

$$S_{12} = \frac{\langle \delta_1 \delta_2 \rangle}{\sigma_1 \sigma_2} \quad (4.6)$$

where $\sigma_i \equiv \langle \delta_i^2 \rangle^{1/2}$ as plotted in Figure 4.7. The cross-correlation of the $n = +3$ N-body density field with the TZA is worse than the other spectra, as one would expect, but better than its cross-correlation with Eulerian linear theory. This shows that “pancake” dynamics are operative even on large scales for $n = +3$. The important difference here is that in the $n = +3$ simulation the correlation

length of the initial potential is vastly smaller than the scale of clustering, and any long-range initial correlations are of extremely small amplitude for $n = +3$. Nevertheless, they appear to dominate large-scale behavior. Also, looking back to the results of the last section, it can be seen that even for $n = +3$, the filaments visible to the eye have correlations in the TZA realizations – not only in the density field, but also in the orientations of specific structures. Generally, based on the correlations in the potential, it has been argued from adhesion theory that coherence in motion would be absent for $n > -1$ (Kofman et al. 1992). These results imply that the adhesion explanation is incomplete, and that the long wave modes of the initial potential dominate motion on scales much larger than R_o .

Perhaps instead the transition from pancake to hierarchical regime takes place, but *gradually* over the entire range of spectral indices from $n = -3$ to $n = +4$. For $n \leq -3$, collapse on all scales happens nearly simultaneously which is a non-controversial sufficient condition for pancaking (Peebles 1980, 1993b). For $n \geq +4$, the minimal k^4 tail from dynamics (Zel'dovich 1965, Peebles 1980) will dominate over initial power. Previous studies have shown that the primary visual change is based on the changing mass of clumps. At $n = -3$, the pancakes are assembled from essentially unclustered matter. As the index n increases, gradually larger clumps are seen. For the $n = +3$ case studied here, there are perhaps two big clumps per pancake which makes it trickier to speak of filaments. Yet the position of these clumps are accurately predicted by the TZA. This means there is coherent motion on scales far exceeding any correlation length in the initial conditions. The extremely low-amplitude power present on very large scales is still enough to dominate the motion.

A simple explanation suggests itself: initial power at high wavenumbers has been essentially “thermalized”, going into binding energy inside clumps. This acts somewhat like smoothing, making the small-scale power unimportant to large-scale structure issues. Of course, the distribution is not smoothed: the high

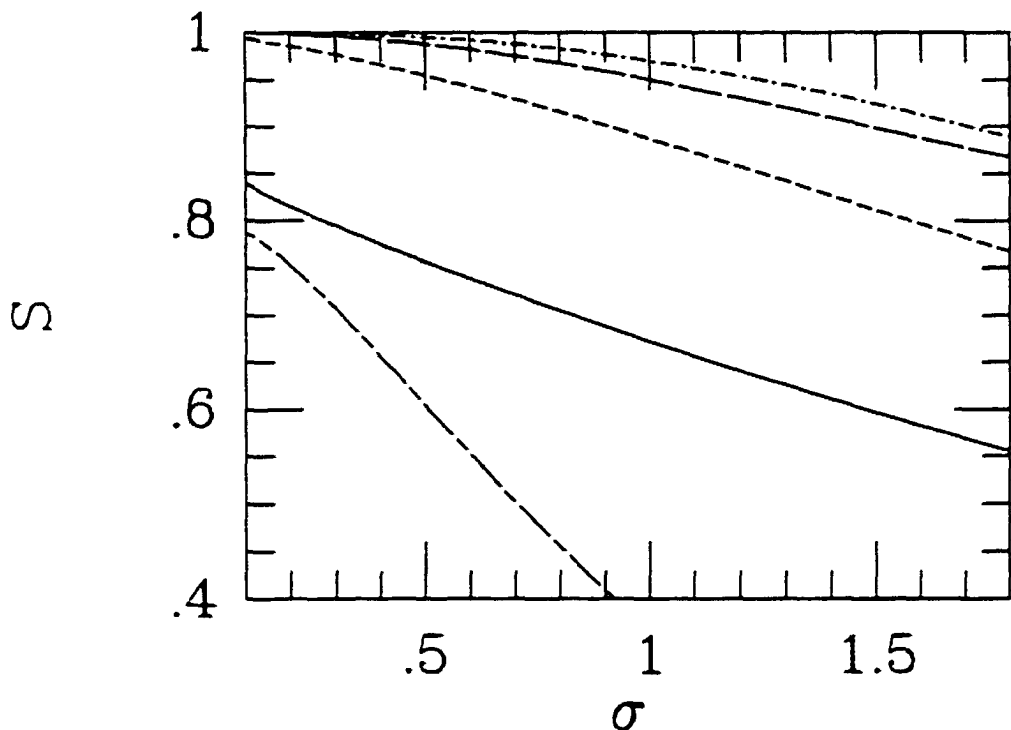


Figure 4.7: Cross-correlation of the smoothed N-body simulations (at $k_{ni} = 8k_f$) with the smoothed TZA against σ of the smoothed N-body density field. In decreasing order of amplitude, $n = -3$ (dot-short dash), $n = -1$ (long dashes), $n = +1$ (short dashes), and $n = +3$ (solid). The lowest line (long dash-short dash) is the cross-correlation of the $n = +3$ simulation with a linear theory extrapolation from its initial conditions and is included for comparison with the TZA performance at $n = +3$.

frequency power exists. But for bulk motion, what counts is power on large scales, which is accurately described in the linear and mildly non-linear regimes by the TZA.

4.4 Conclusions

The Zel'dovich Approximation based on the smoothed initial gravitational potential (TZA) works with continuously changing accuracy over the range of spectral indices $-3 \leq n \leq +3$. There are no sudden jumps in behavior, so that the transition from pancaking to hierarchical clustering is continuous. Therefore the TZA can be used to predict (via the eigenvalues and eigenvectors of the deformation tensor) the orientation and relative oblateness or prolateness of sheets and filaments that arise in N-body simulations of hierarchical clustering.

4.5 References

- Babul A. & Starkman G. D. 1992. ApJ, 401, 28
Coles P., Melott A. L., & Shandarin S.F. 1993. MNRAS, 260, 765
Gurbatov S. N., Saichev A. I., & Shandarin S. F. 1989. MNRAS, 236, 38
Kofman L., Pogosyan D., Shandarin S. F., & Melott A. L. 1992. ApJ, 393, 437
Melott A. L., Pellman T. F., & Shandarin S. F. 1994, MNRAS, 269, 626
Melott A. L. & Shandarin S. F. 1993, ApJ, 410, 469
Peebles P. J. E. 1980, *The Large-Scale Structure of the Universe*, (Princeton University Press, Princeton NJ)
Peebles P. J. E. 1993a. in *Cosmic Velocity Fields*, eds Bouchet F. R. & Lachieze-Rey K., (Editions Frontiers, Gif sur Yvette, France)
Peebles P. J. E. 1993b, *Principles of Physical Cosmology*, (Princeton University Press, Princeton NJ)

van Haarlem M. & van de Weygaert R. 1993, ApJ, 418, 544

Zel'dovich Ya. B. 1965, Adv. Astron. Ap., 3, 241

Chapter 5

Evolution of the Gravitational Potential

5.1 Introduction

There have been hints before that gravitational clustering acts like a smoothing of the gravitational potential (see Press & Schechter 1974; Melott, Weinberg, & Gott 1988; Weinberg & Gunn 1990; Little, Weinberg, & Park 1991; Kofman et al. 1992). This not only suggests an explanation for the success of the TZA, which consists of moving particles by the ZA in a smoothed version of the initial potential, but it could also explain why the TZA works outside the regime in which adhesion theory implies it should. Adhesion theory concerns itself with the initial potential, which will be shown to evolve considerably. It will further be shown that this evolution may be described quite well by smoothing, and that for $n = +1, +3$ the smoothed initial potential looks nothing like the unsmoothed initial potential but does resemble the *unsmoothed evolved* potential. For $n = -1, -3$ the potential does not evolve much, so the smoothed and unsmoothed initial and unsmoothed final potentials all resemble one another.

¹This chapter was taken largely from Pauls J. L. & Melott A. L., 1995, MNRAS, 274, 99.

5.2 The Initial and Final Gravitational Potentials

In Figure 5.1 one diagonal cut through the gravitational potential of the initial and evolved ($k_{nl} = 8k_f$) simulation cubes are shown superimposed. To linear order the potential is constant. For $n = -1, -3$ the potential evolves very little. This is because the power spectral index of the potential is $n-4$, from the Poisson equation: it is dominated by the low- k linear modes in both cases. Of course the potential here is dependent on the low- k cutoff (the fundamental mode), and a larger box would immediately give rise to a larger oscillation. This would only reinforce the similarity between initial and evolved potential. This lack of evolution makes all sorts of approximation schemes work well (Melott 1994) for $n \leq -1$.

For $n = +1, +3$ the situation is quite different. The divergences in the gravitational potential are only logarithmic for $n = +1$ but are strong at high- k for $n = +3$. The initial potential shows the usual high frequency oscillations and is dominated by them for $n = +3$. More resolution would give rise to even more violent oscillations. In this case, however, the unsmoothed evolved potentials are very different. They display almost no hint of the fine structure present in the initial conditions. In this sense, gravitational clustering has “smoothed” the potential. The gravitational evolution of topological genus also gives hints of smoothing (Melott et al. 1988). Can this idea be pushed a step further? In Figure 5.3 the *smoothed* initial potential is explicitly compared to the *unsmoothed* evolved potential. The initial potential is smoothed in exactly the same way it is smoothed to implement the TZA – i.e. Gaussian convolution with the optimal window (Eq. 2.8) for a given power spectral index. The agreement is remarkable, considering the deeply nonlinear evolution and the very small initial amplitude of the long waves.

In order to make slightly more quantitative this claim about the potentials,

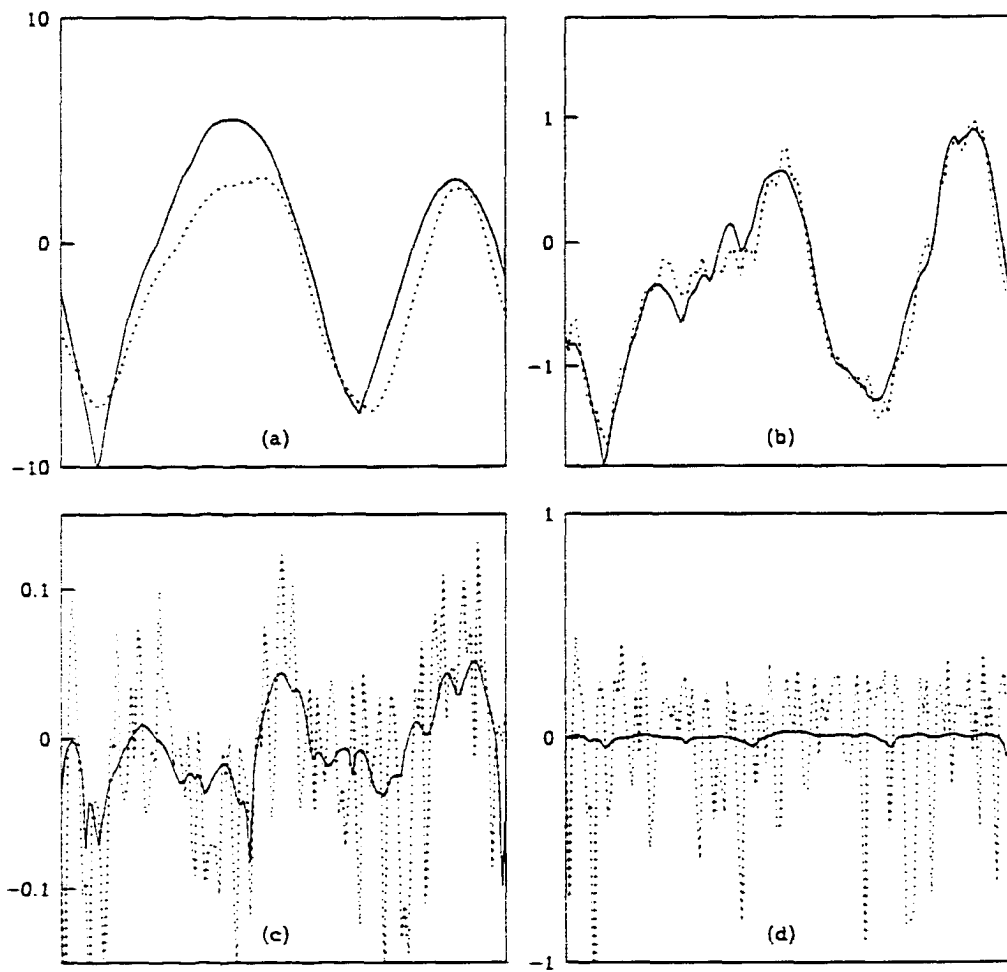


Figure 5.1: The peculiar gravitational potential is shown along one diagonal of each of the four simulation cubes (a) $n = -3$, (b) $n = -1$, (c) $n = +1$, (d) $n = +3$. The units are arbitrary but do reflect that the potential is constant to linear order. Note that there is strong evolution in the potential for $n = +1, +3$, but not for $n = -3, -1$. Solid line shows the potential evolved to $k_{nl} = 8k_f$. Dotted line shows the initial potential.

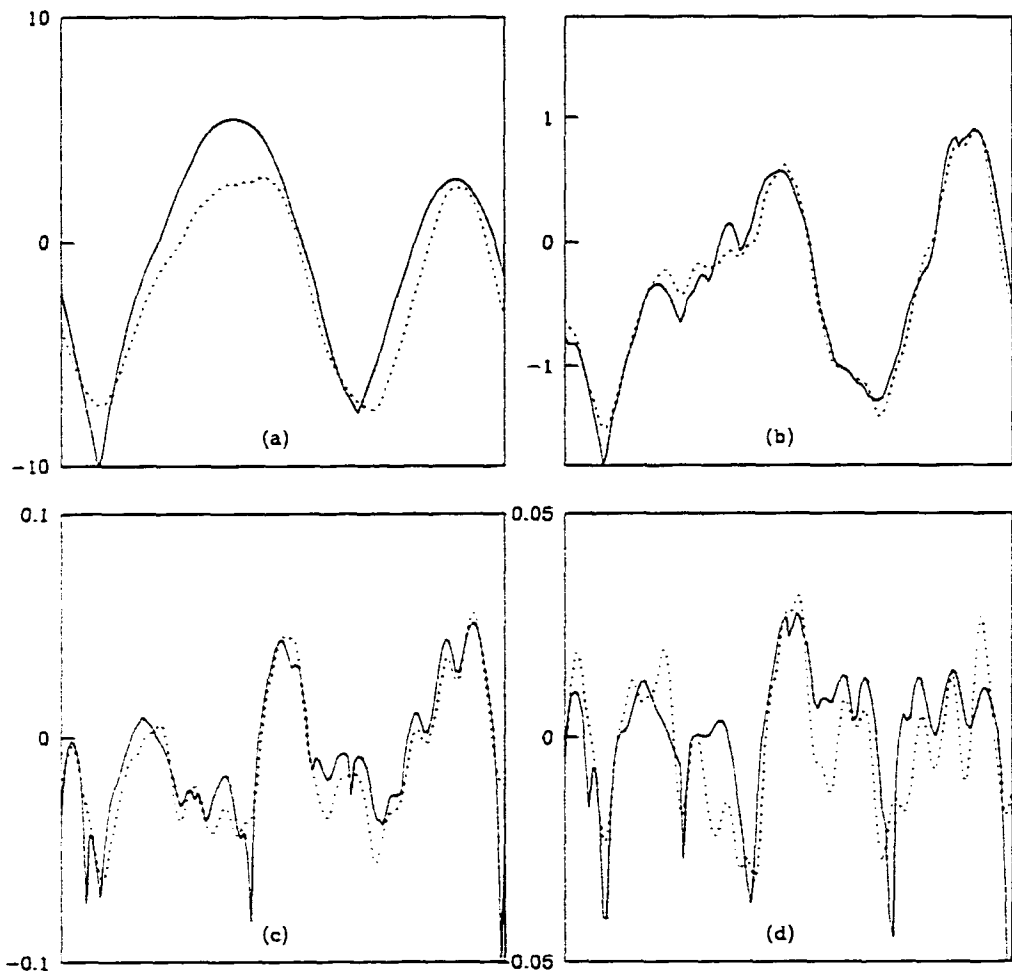


Figure 5.2: The peculiar gravitational potential is plotted in the same manner as in Figure 5.1, except that the initial potential only has been smoothed with the same Gaussian used in the TZA (Equation 2.7). The smoothed initial potential strongly resembles the unsmoothed potential in the nonlinear regime. Note: for the case of $n = -3$, the optimal smoothing was no smoothing, so Figure 5.2a is identical to Figure 5.1a; also, the vertical scales have been changed for Figures 5.2c,d as compared with Figures 5.1c,d.

Table 5.1: Cross-correlation of gravitational potentials.

Spectral Index	Smoothed Initial	Initial/Initial	Initial/Final	Smoothed Initial	Initial/Final
-3	-		0.96	-	
-1	0.999		0.987	0.990	
+1	0.68		0.65	0.94	
+3	0.14		0.10	0.69	

the cross-correlation coefficient (see Eq. 4.6) was computed for the peculiar gravitational potentials on the 128^3 mesh. In Table 5.1 the cross-correlations between pairs of the three fields for each spectral index - initial, optimally smoothed initial, and final ($k_{nl} = 8k_f$) are shown. The case of $n = -3$ is shown for reference only.

For $n = -3, -1$, all cross-correlations are large. This is a simple consequence of the strong emphasis on small- k modes in the potential. There is a small improvement in the third significant figure for $n = -1$. The cases of $n = +1, +3$ are much more interesting. In these cases the smoothed initial potential is *much* more strongly correlated with the final (nonlinear) potential than is the raw initial potential. This is not just an artifact of removing high-frequency power, as shown by the cross-correlation of the smoothed initial potential with itself (unsmoothed). This is a quantitative measure of the fact that the evolved potential resembles the smoothed initial potential, as seen in Figure 5.3. Although mass density and gravitational potential are related by the Poisson equation, this resemblance is not true for the mass density: the evolved mass density does *not* resemble the linearly amplified smoothed initial mass distribution (Coles et al. 1993). Those correlation coefficients were less than 0.1 for $n = -1, +1$.

5.3 Implications for Approximations

The ZA of course uses the potential to move the particles. The unexpected accuracy of the TZA is explained by the fact that the smoothed initial potential

Table 5.2: Coherence length (in cell units) of the gravitational potential for the spectral indices discussed.

Spectral Index	initial	$k_{nl} = 8k_f$
-3	36.0	36.0
-1	31.5	31.5
+1	1.7	7.6
+3	0.6	4.2

resembles the evolved potential, even for $1 \leq n \leq 3$, allowing the TZA to work reasonably well. The potential in which the clumps move has a lot of long-range coherence. This becomes true, even if it was not true in the initial conditions.

In Table 5.2 the coherence length of the potential in the initial conditions and at the stage $k_{nl} = 8k_f$ is shown. It is defined as the radius at which the auto-correlation falls to half its value at the smallest radius that can be resolved. For $n = +3$, the coherence length is entirely dependent on the large- k cutoff, and will become arbitrarily small as the resolution is increased. For $n = -1, -3$ the coherence length will become large as the box size is increased, since in these models it is dominated by the long waves.

It is changes that are sought. For $n = -3, -1$, the coherence length changes very little. In both cases the numerical limitation is at small k (the longest waves). It seems safe to assume that it would not evolve in a much larger box. For $n = +1, +3$ the coherence length increases by a factor of 7 to 8 as gravitational clustering proceeds. The initial length is quite small, while the evolved length is comfortably within the dynamic range of the box. This growth of the coherence length of the evolved potential shows why bulk motions are coherent and lead to “superpancakes”.

This behavior suggests new approximations which may be worthwhile. Particle-pushing versions of adhesion (Weinberg & Gunn 1990) as well as the Frozen Potential Approximation (Brainerd, Scherrer, & Villumsen 1993; Bagla & Padmanabhan 1994; Sathyaprakash et al. 1995) move particles in some way in the initial

potential. Adhesion did not do as well as the TZA for $n > -1$, while the Frozen Potential Approximation did not do as well for any indices in various tests. New improved versions of these approximations should be constructed which move the particles at each step in the variably *smoothed* initial potential. This is not to suggest that they will be cost-effective replacements for N-body simulations, but that they should add to our understanding of clustering.

One group (Melott et al., 1996) has implemented this suggestion. They created an improved version of the Frozen Potential (FP) approximation, called the Step-wise Smoothed Potential (SP) approximation. In this approximation, particles are moved at a number of timesteps, as in N-body models. However, the potential used to move the particles is a version of the initial potential, smoothed at each timestep with a optimized Gaussian window $e^{-k^2/2k_G^2}$ where $k_G \sim k_{nl}$. Their test was done for 2D models with $n = +2, 0$ (which corresponds to 3D models with $n = +1, -1$). The comparison of the SP and FP with N-body results can be seen in Figure 5.3. In more quantitative comparisons, they found that the SP out-performed the Adhesion approximation (AA) and FP (but not the TZA) in density cross-correlation (Eq. 2.7). When particle displacement was considered, the SP outperformed all tested approximations, *including* the TZA.

5.4 Conclusions

The agreement of the nonlinear potential with the smoothed initial potential in an evolved hierarchical clustering simulation is nontrivial. The evolved mass density field does *not* resemble the smoothed initial mass density field (Coles et al. 1993) or the initial potential field, either smoothed or unsmoothed. This smoothing of the potential justifies the use of and explains the performance of the Zel'dovich Approximation with smoothed initial conditions (TZA). A new understanding of galaxy and large-scale structure formation can be developed by combining the hierarchical and pancake approaches which were formerly thought to be mutually

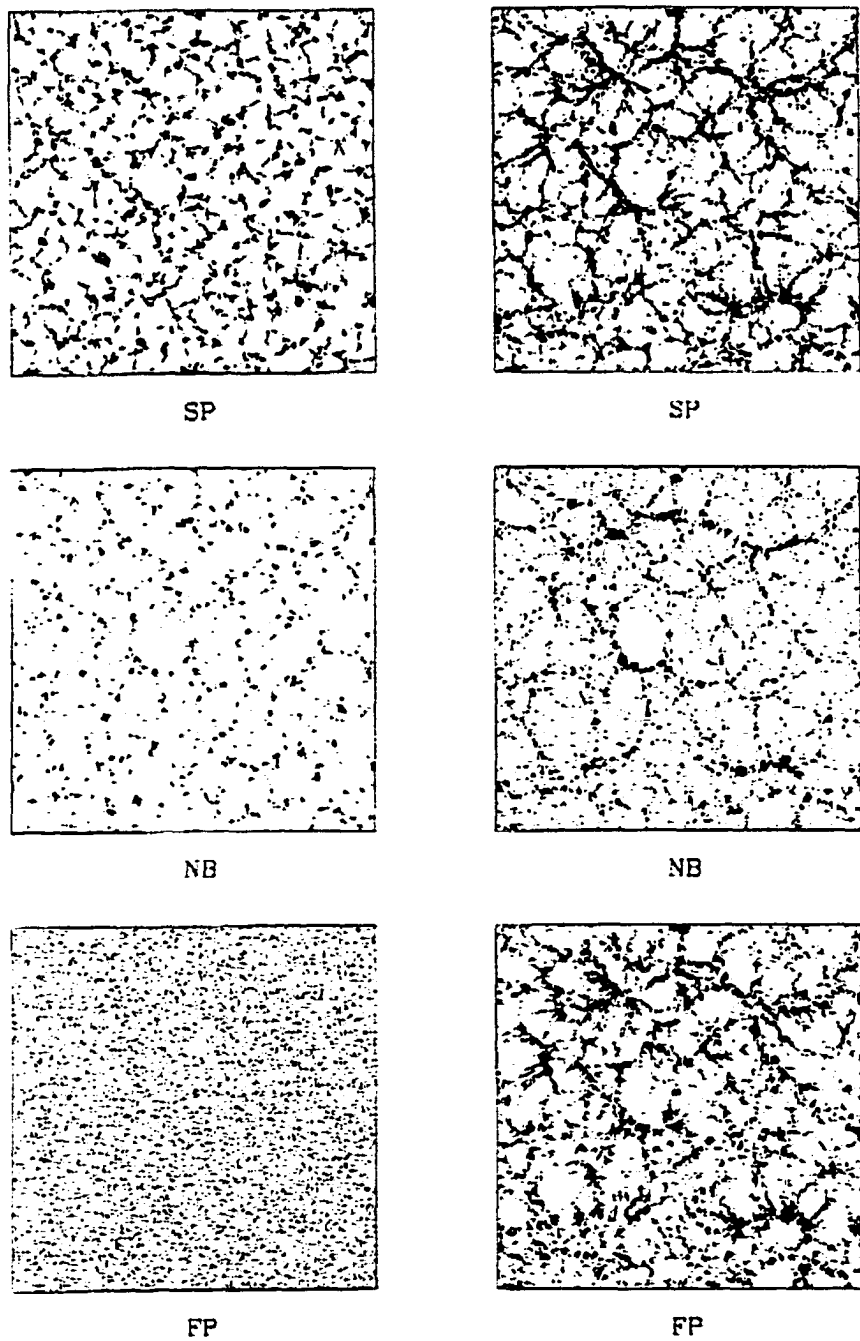


Figure 5.3: Plots showing the particle positions at $k_{nl} = 8k_f$ from three different models of the same initial conditions. The top row shows the Smoothed Potential; the middle shows the N-Body (for comparison); and the bottom shows the Frozen Potential. Left (right) side shows results for $n = +2$ (0) 2D models. (Melott et al.. 1996: reprinted by permission.)

exclusive. By doing this, the coherence of motion which leads to hierarchical pancaking can be explained, providing an explanation for the visually rich large-scale structure of the Universe.

5.5 References

- Bagla J. S. & Padmanabhan T. 1994, MNRAS, 266, 227
Brainerd T. G., Scherrer R. J., & Villumsen J. V. 1993, ApJ, 418, 570
Coles P., Melott A. L., & Shandarin S. F. 1993, MNRAS, 260, 765
Little B., Weinberg D. H., & Park C. B. 1991, MNRAS, 253, 295
Kofman L., Pogosyan D., Shandarin S. F., & Melott A. L. 1992, ApJ, 393, 437
Melott A. L. 1994, ApJ, 426, L19
Melott A. L., Sathyaprakash B. S., & Sahni V. 1996, ApJ, 456, 65
Melott A. L., Weinberg, D. H., & Gott J. R.. 1988 ApJ, 328, 50
Pauls J. L. & Melott A. L. 1995, MNRAS, 274, 99
Press W. H. & Schechter P. 1974, ApJ, 187, 425
Sathyaprakash B. S., Sahni V., Munshi D., Pogosyan D., & Melott A. L. 1995,
MNRAS, 275, 463
Weinberg D. H. & Gunn J. E. 1990, MNRAS, 247, 260

Chapter 6

Three-Point Correlation Function and Triple Lines-of-Sight

6.1 Introduction

As was seen in Chapter 3, gravitational collapse tends to give us sheet-like structures. It is believed that such sheets are seen in large galaxy surveys such as the Las Campanas survey (Fig. 1.1). To see these sheets, it is necessary to look at a number of adjacent slices (available in Shectman, et al., 1996). If one does this, it can be seen that the long thin structures in the 2D slices are really cross-sections of large thin sheets in 3D.

More recently, there has been interest in determining the characteristics of large hydrogen clouds that appear in the spectra of Quasi-Stellar Objects (QSO's) with small angular separations. Dinshaw et al. (1995) and Bechtold et al. (1994) have examined the spectra of such closely-spaced QSO pairs as those shown in Figure 6.1 and noted that a large fraction of lines in one spectra are coincident with lines in the other (for example, line #2 in the spectra of Q1343+266A is

coincident with line #2 in the spectra of Q1343+266B, line #6 in A is coincident with #3 in B, etc.). Based on these coincidences, the anti-coincidences (lines without partners), and the separation of the lines-of-sight, they conclude that these large clouds have proper scales $40\text{-}310 h^{-1}$ kpc, assuming a value of the deceleration parameter, $q_0 = 0.5$ (this is equivalent to co-moving sizes $110\text{-}870 h^{-1}$ kpc at the redshifts of their QSO's). If $q_0 = 0$, these values are increased by 50%. More recently, Crotts (1997) has studied other spectra and suggests that these gas clouds are even larger ($\sim 0.5 h^{-1}$ Mpc or larger) and two dimensional.

Lyman-alpha is the designation given to the transition in a hydrogen atom as its electron moves from the ground state to the first excited state or back down again. A Lyman-alpha absorption line is, then, an absorption line (in a spectrum) caused by light passing through a cloud of neutral hydrogen. If a QSO, or another object at a substantial redshift, is selected to be a light source, then absorption features in its spectrum may be used to tell whether or not there is any neutral hydrogen between it and us. Further, by examining the wavelengths at which Lyman-alpha absorption features occur, the redshift of (and, therefore, the approximate distance to) the intervening hydrogen cloud(s) may be inferred. Since the Universe is made up primarily of hydrogen (roughly three-quarters of the baryonic mass is in hydrogen), knowing the shapes and extents of these hydrogen clouds may provide critical insight to the dynamics of structure-formation.

The information about hydrogen clouds in the spectrum of a single QSO is clearly one dimensional, but it can be used to recover information about the 3-D structure of the clouds. Consider the objects located using the spectra of three QSO's which have small angular separations (Figure 6.2). It can easily be imagined that if these objects are large and flat, all three lines of sight will often intersect a single object. If, on the other hand, these objects are more pointlike, it will be much less likely to find coincident structures in the three lines. In the intermediate case of filamentary structures, it would be expected that some

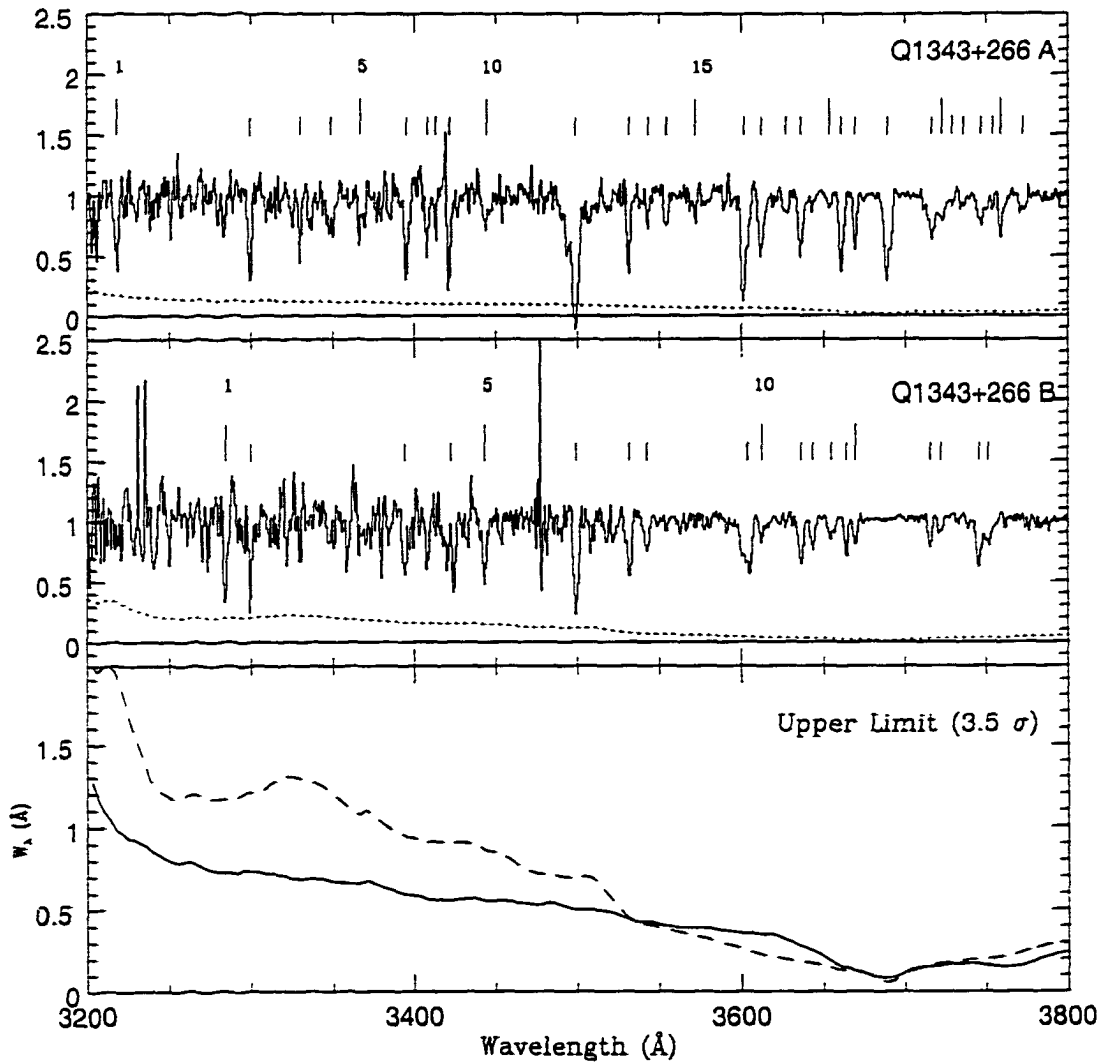


Figure 6.1: The upper two panels show spectra of the Lyman-alpha forest of the QSO pair Q1343+266 A, B. Tick marks show significant absorption features. The dotted line shows 1σ errors. The lower panel shows the observed equivalent width threshold (3.5σ) for an unresolved line as a function of wavelength for A (solid line) and B (dashed line). (Bechtold et al., 1994; reprinted by permission.)

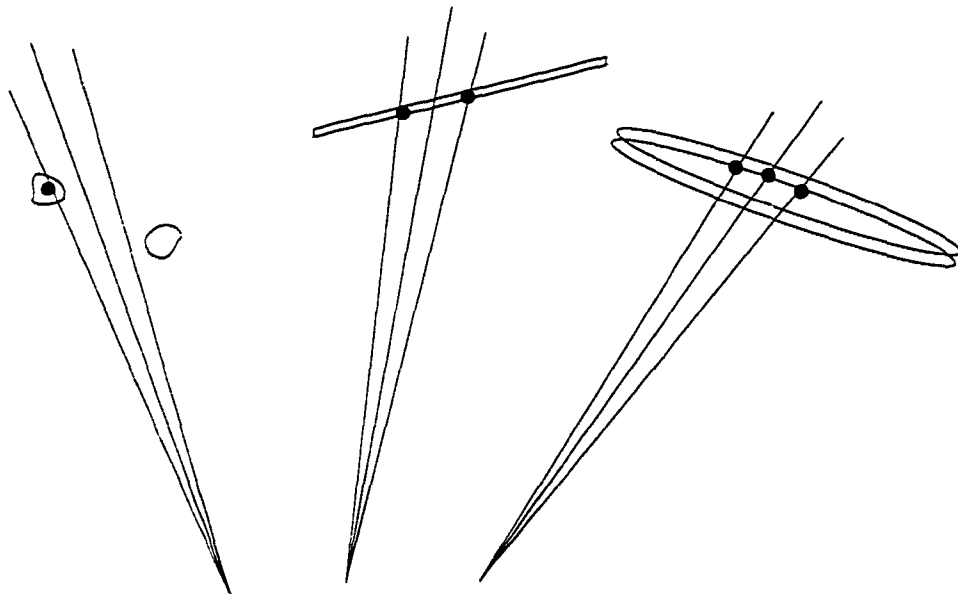


Figure 6.2: Simplified sketch of three possible geometries: point/clumpy, line/filamentary, and disk/sheet-like. The lines-of-sight form a triangle (in 3D) and their intersections with the objects are marked with black dots.

coincidences would be found in two of the lines of sight, but not all three. To quantify this idea, the 3-point correlation function is adapted to this triple-line-of-sight (hereafter TLOS) data form and the reduced three-point correlation function is calculated for data drawn from several numerical models. I will show that it is possible to distinguish models which are characterized by sheets from those that are not based on this 1-D information.

6.1.1 2- and 3-Point Correlation Functions

The idea behind the n -point correlation functions is that there are informative ways to split up the probabilities that something will happen into 1-, 2-, 3-, and n -dependent ways. The “one-point correlation function” is not generally spoken of, but is basically just the probability that you will find an object in a random volume element in a distribution:

$$dP = n dV \quad (6.1)$$

where dP is the differential probability of finding an object that is part of a distribution of number density n in a differential volume dV .

The discussion becomes more interesting when we move on to correlated probabilities in the two-point distribution function:

$$dP = n^2 dV_1 dV_2 (1 + \xi(r_{12})) \quad (6.2)$$

now dV_1 and dV_2 are two differential volumes separated by a distance r_{12} and dP represents the joint probability that there will be objects found in *both* of these volumes. This probability can be broken up into two parts – the two terms in the parentheses. The “1” is the part of the probability that there will be two objects found in a *random* distribution. The 2-point correlation function, ξ , is the other part: the part in excess of random, the part due to “real” 2-point clustering effects (or, if $\xi < 0$, the anti-clustering effects). Of course the expression containing the three-point correlation function may be analogously written:

$$dP = n^3 dV_1 dV_2 dV_3 (1 + \xi_{12} + \xi_{23} + \xi_{31} + \zeta_{123}). \quad (6.3)$$

Again the “1” is due to the probability of finding randomly scattered objects in all three differential volumes. The ξ_{ij} terms each represent the probability that there will be a real 2-point correlation effect in volumes dV_i and dV_j , and a random coincidence in the third differential volume. It is only ζ_{123} , the *reduced* three-point correlation function, that represents the real 3-point clustering (or anti-clustering) effects.

The one-point correlation function is really only useful for giving us information about the number density of objects. The two-point correlation function is useful for returning information about a characteristic scale of clustering (or lack

of clustering). I will show that the reduced three-point correlation function can give information about the basic geometry of objects.

6.2 Method

6.2.1 Background

The statistics developed in this section were applied to two classes of simulations and there are plans to test them with real data, when enough becomes available. The first class is N-body simulations. These were done in 3-D with spectral indices $n = -2, -1, +1$, and power on all resolvable scales. The second class of simulations was toy models – one with mass in points, one with mass in filaments, and one with mass in disks. All shapes were randomly distributed, and the filaments and disks were also randomly oriented. The mass was evenly distributed in “perfect” realizations of the shapes (that is, within roundoff error of the computer, the points were of zero dimension; the filaments of one dimension; and the disks of two dimensions), then these perfect mass distributions were placed on the same 128^3 mesh as the simulations and smoothed on a scale of one grid cell. They were designed to have scales comparable to the N-body simulations, and the number of objects was adjusted (while the total mass was held constant) to give the same correlation length as their N-body counterparts. For purposes of adjusting the models, the correlation length was calculated using full 3D mass information. The toy models were included to show that the 3-point function is able to distinguish the dimensionality of the structures.

Since the QSO data being roughly mimicked here is in the form of a list of identified lines at known redshifts with assigned significance levels, the simulations must be manipulated to give data in a compatible format. Absorbers are identified in the simulations as cells with density above some threshold. A string of cells, all with density above the threshold, is seen as one absorber, whose position is at the

center of mass. By adjusting the threshold, it will be possible to obtain a given number of absorbers per line of sight (which can be scaled to unit distance). In the real data, the significance level may be similarly adjusted to match the desired number of absorbers per unit distance. Further, the 2- and 3-point functions may be compared over a range of number densities of absorbers. Higher number densities will be consistent with low density/significance level thresholds and lower number densities will be consistent with high density/significance level thresholds. In this way, the effect of biasing on the results can be seen.

The idea of 2- and 3-point correlation functions is adapted to fit the form of the data. Because complete spatial information will be unavailable in the real data to be analyzed, the co-moving separations of the lines are fixed (instead of fixing the separations of volume elements). The coincidences along the two lines of sight are counted by looking along one line of sight (hereafter LOS) until an absorber is found. Then a coincidence is searched for in another LOS anywhere inside a window, whose length is determined by the overall scale of the model. This differs from the standard 2- and 3-point correlation functions in that (1) the (primary) independent variable is the number density of absorbers (based on density/significance threshold) and (2) the separation is fixed in one (2-point) or two (3-point) dimensions and given a range $r \leq w$ in the other dimension, where w is the windowsize. In contrast, the separation r is completely fixed in the usual 2- and 3-point functions. This is shown in Figure 6.3.

Absorbers along a LOS are identified as described above for a range of density levels. Then the absorbers are counted and the average number of absorbers along a LOS, n (this will later be normalized to a number density), is calculated.

The next task is to define the windowsize. This is the size of a window around an absorber in one LOS in which an absorber in another LOS (see Figure 6.4) is defined as coincident. (Clustering effects along a single LOS are ignored.) This windowsize is selected based on the scale of a particular realization: for

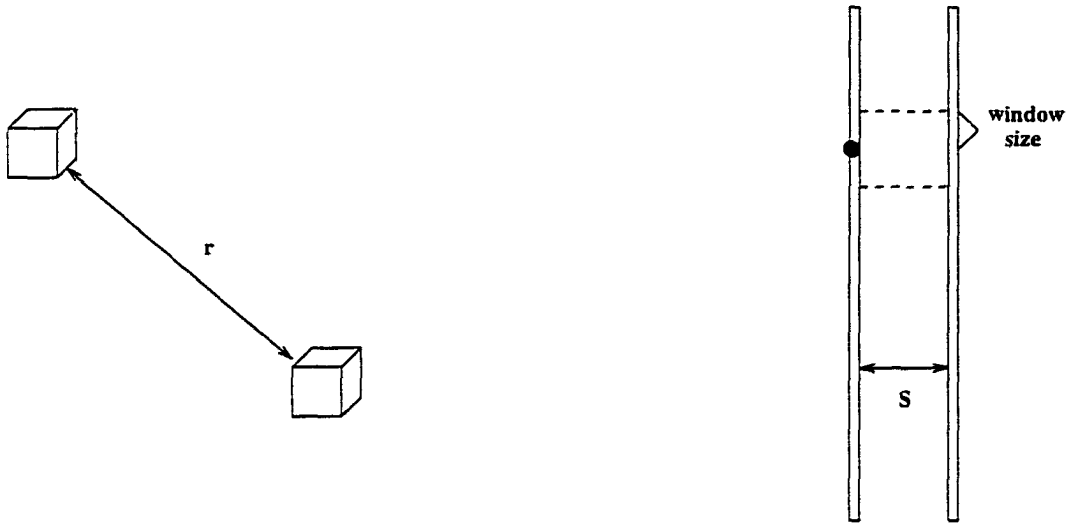


Figure 6.3: Change in the format of the data of the 2-point correlation function. The left shows the usual data format: two differential volumes separated by a distance r . The right side shows my data format: two LOS separated by a distance S . An absorber is shown marked with a black dot. If there were an absorber in the second LOS within the window (above or below), it would be counted as a coincidence.

a realization characterized by small structures, a small window is chosen: one with larger structures gets a larger window. The size of these windows is set to correspond to the scale of the objects just becoming nonlinear.

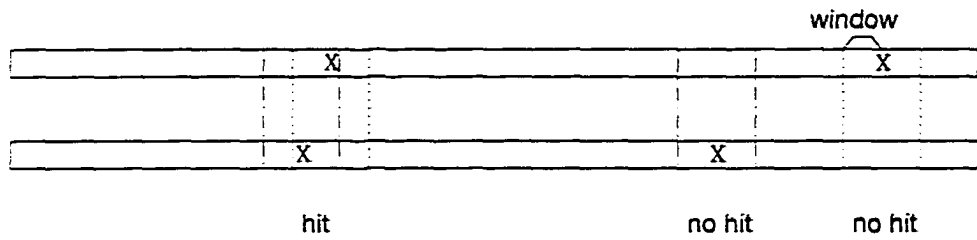


Figure 6.4: A typical picture of a double LOS with two absorbers (marked with "X"'s) along each LOS. The vertical dotted lines show the extent of the windows around each absorber. There is one hit/coincidence, which is marked.

While the independent variable for calculations is density, it can be related to n , the average number of absorbers/LOS in the simulation. Further, the results of Melott & Shandarin (1993) can be used to find the co-moving scales for the simulation boxes (see Table 6.1). The toy models are comparable to the $n = -1$

Table 6.1: Scales of N-body models. All distances are co-moving.

Spectral Index	Box Size h^{-1} Mpc	Cell Size h^{-1} Mpc	Characteristic Structure Size h^{-1} Mpc (cells)
-2	190	1.5	6.6 (4.5)
-1	170	1.3	4.3 (3.3)
+1	140	1.1	2.8 (2.6)

model. For comparison, the triplet reported by Crotts (1997) has a proper separation of $0.5 - 0.7 h^{-1}$ Mpc at a redshift of 2.5. This corresponds to a separation of 1-2 cells in my simulations. This scaling will allow us to use $n/100h^{-1}$ Mpc, the variable most appropriate for doing comparisons with real Lyman- α data, as the independent variable for plotting our results.

6.2.2 Random Coincidences

For the 2-point analog (hereafter 2PA) two cases are considered. The first is the case in which $n \leq 1$. In this case, the probability that there will be many overlaps of absorber windows (within a single LOS) is very low. The probability that there is a randomly placed absorber in the second LOS that is in the window of a given absorber in the first LOS is

$$P_{2rand}(n, w) = n \times 2(w/L). \quad (6.4)$$

The subscript refers to the number of LOS under consideration and the fact that this is the part of the probability due to random coincidences; L is the boxsize.

This simplistic approach breaks down when nw becomes an appreciable fraction of the boxsize and the correct solution becomes a recursive expression. Letting n be the number of absorbers in a LOS, (n must be an integer here), the probability that there will be a coincidence for a known absorber in another LOS will be

$$P_{2rand}(n=1, w) = 2(w/L) \quad (6.5)$$

if there is *one* absorber in the line being searched. For each additional absorber in the searched line, the probability of a coincidence increases:

$$P_{2rand}(n, w) = P_{2rand}(n-1, w) + P_{2rand}(1, w)(1 - P_{2rand}(n-1, w)). \quad (6.6)$$

To accommodate non-integral values of n (which represents an *average* number of absorbers per LOS), one can calculate the probabilities for the integers immediately above and below n and interpolate, which was done.

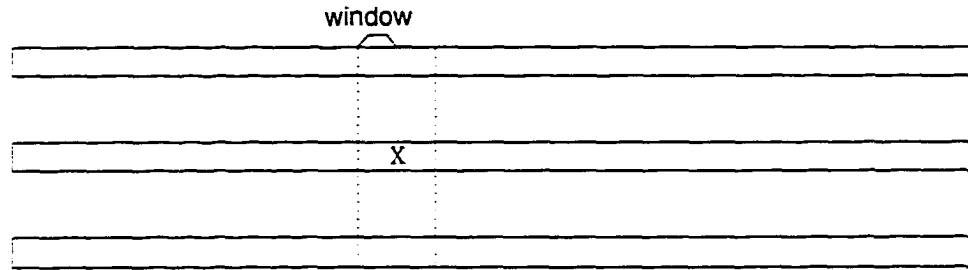


Figure 6.5: An example of three LOS, with one absorber marked in the middle line.

Now the same thing is done for the 3-point analog (hereafter 3PA). Consider again two LOS, with a third LOS between them (Figure 6.5). From the 2PA, the probability that an absorber will be found in the upper LOS for a given absorber in the middle LOS is known to be $P_{2rand}(n, w)$. This is the same as the probability that a coincident absorber in the lower LOS for that same absorber in the middle LOS will be found. So the joint probability (for a random distribution, which is the term of interest here) is the product of the two, $P_{2rand}(n, w)^2$. However, there's a complication: the absorbers coincident in the upper and lower LOS's may *not* be within one window length of each other (Fig.6.6). A careful examination of

the possible cases, leads to the amended equation:

$$P_{3rand}(n, w) = \frac{3}{4} P_{2rand}(n, w)^2. \quad (6.7)$$

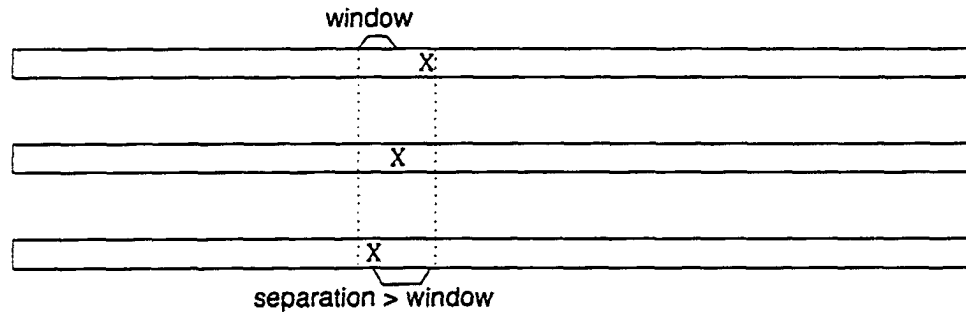


Figure 6.6: An example of three LOS, with one absorber marked in the middle line. The absorbers in the upper and lower lines are each coincident with the absorber in the middle line, but not with each other. This is *not* an example of a triple coincidence.

6.2.3 Real Coincidences

The probability of finding coincidences in the simulations or the real data does not have an analytic expression, the coincidences must actually be counted. As mentioned before, this is done by looking down one LOS until an absorber is found, then looking down the other one (or two) LOS for coincidences. The probability of finding a double (P_2) or triple (P_3) coincidence (given that we began on an absorber) is then the total number of coincidences divided by the number of absorbers down the first LOS. Now the two- and three-point equations look like this:

$$P_2 = P_{2rand}(1 + \xi_{12}) \quad (6.8)$$

and

$$P_3 = P_{3rand}(1 + \xi_{12} + \xi_{23} + \xi_{31} + \zeta_{123}). \quad (6.9)$$

and we can solve for ξ_{ij} and ζ_{123} . The results are presented for different separations of the LOS. For the 2-point function, these separations are exact: $S = 1$ cell means the LOS are adjacent; $S = 2$ cells means there is one cell separating the LOS, etc. For the 3-point function however, the grid makes exactly even separations impossible. Consequently, the best approximation to an equilateral triangle is made. For $S = 1$ cell, the true separations are 1 cell, 1 cell, and $\sqrt{2}$ cells; for $S = 2$ cells, the separations are 2 cells, $\sqrt{5}$ cells, and $\sqrt{5}$ cells, etc. While the current TLOS work assumes three (reasonably) evenly-spaced LOS, there is nothing special about this case other than it allows a discussion of results on specific scales. These statistics could easily be adjusted to any three relative separations desired. Indeed, it is unlikely that the real data will be found in such evenly-spaced orientations.

6.3 Results

Since the simulations have power-law power spectra, they are scale-free. The stage of evolution may be selected to correspond to whatever overall box size is desired. The results presented are for an intermediate evolution, $k_{nl} = 8k_f$ where k_f is the fundamental mode of the box. This stage is late enough to see reasonably-sized non-linear structures with good resolution, but not so late that the model box contains only a few structures.

6.3.1 Two-Point Correlation Function Results

First results from the two-point correlation function (Figures 6.7 and 6.8) are considered and several LOS separations (1, 2, 4, and 8 cells) are shown. The 2-point correlation function is expected to be very strong when the LOS are separated by only one cell, as it is, but since this separation is at the resolution limit of the simulation, these results should not be considered entirely reliable. At the

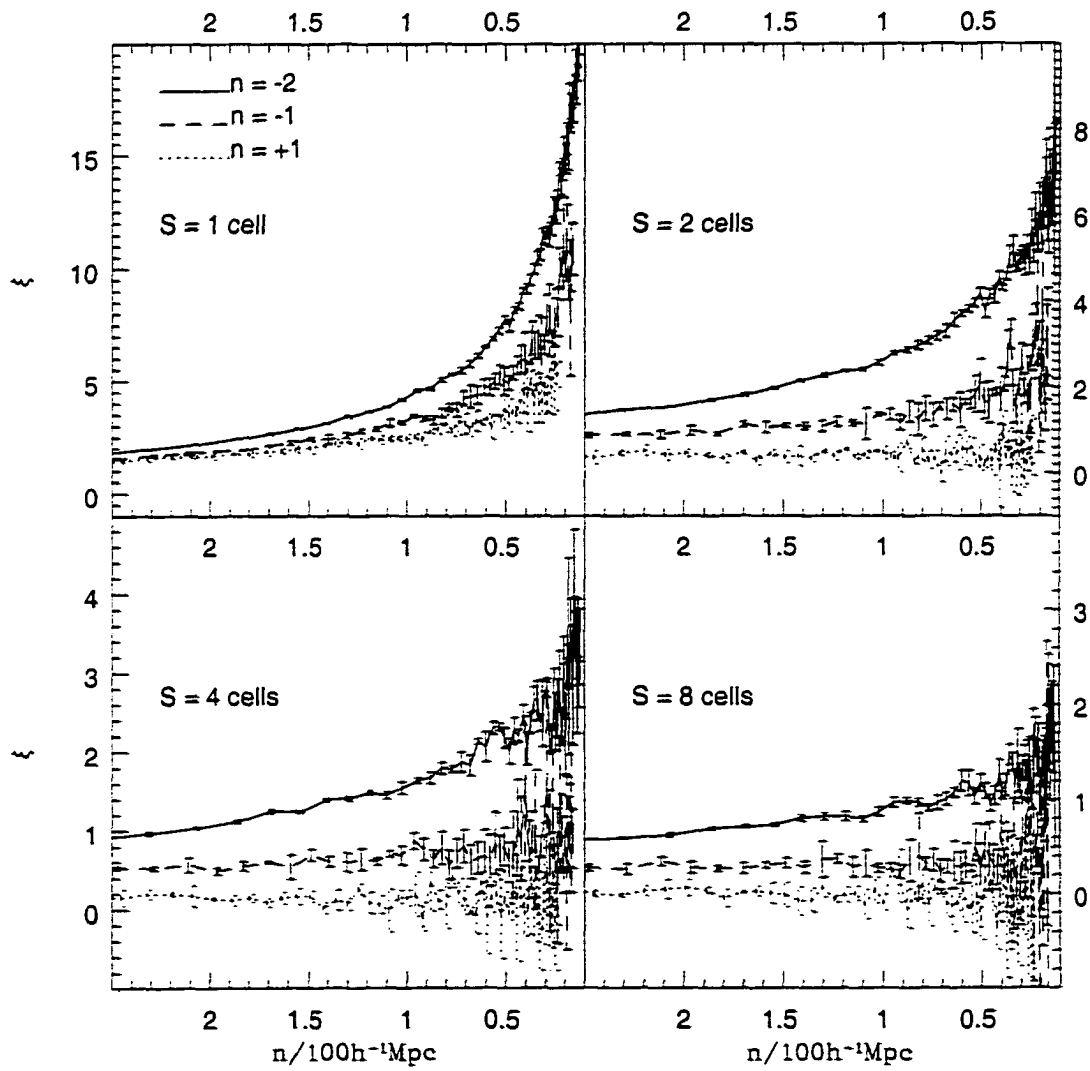


Figure 6.7: The 2-point correlation function for three N-Body models. S is the separation of the LOS in cells. The range of number density of absorbers corresponds roughly to $1.5 \leq \delta \leq 16+$.

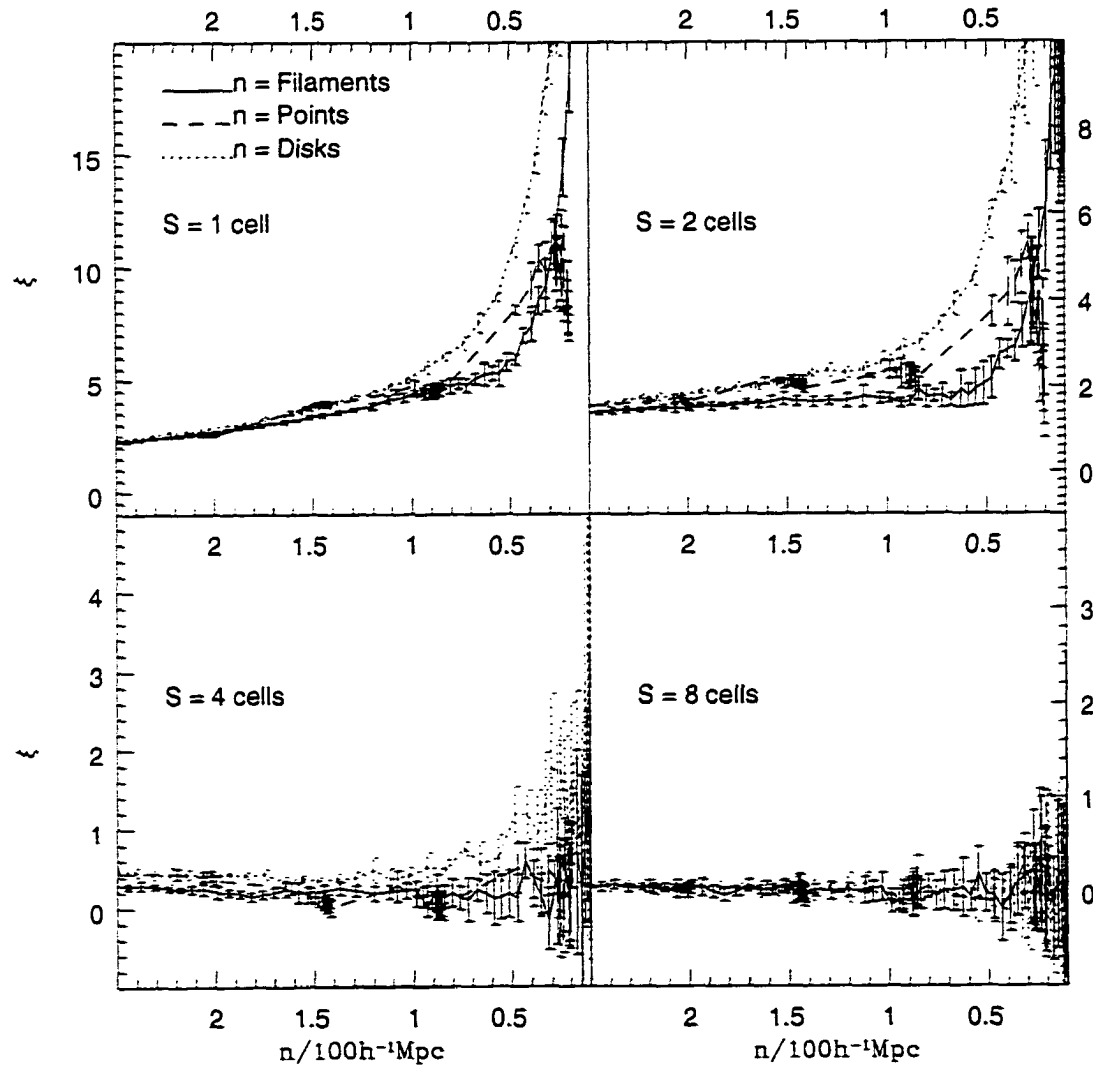


Figure 6.8: As in Figure 6.4 for three toy models. The range of number density of absorbers corresponds roughly to $2 \leq \delta \leq 10$.

other extreme, eight cell separation shows only a very slight positive signal for the $n = -1, -2$ models and no signal for the other models. (Since $\xi = 0$ for a random distribution, a non-zero value of ξ is referred to as a signal.) This is also expected, since the scale just becoming non-linear in the simulations at this stage is between four and eight cells. The interesting, and relevant, LOS separations at this stage/scale are two and four cells. In the N-body models, there is a definite trend – the $n = -2$ model has a consistently higher 2-point function than the $n = -1$ model, which in turn is consistently higher than $n = +1$. This is to be expected. Refer back to the slices shown in Figure 4.1. They show the definite trend from extremely clumpy structures at $n = +3$ to more filamentary and sheet-like structures at $n = -3$ (though the distinction between sheets and filaments cannot be made from the single slices shown). This transition mirrors the trend of the power spectra to have more power at larger scales (and therefore more connected structures) as the spectral index decreases. This can also explain the slight signal for the $n = -1, -2$ models with 8 cell LOS separation – some large scale power (and more for $n = -2$ than for $n = -1$ model) is present in them, giving them a small, but measurable, value of the two-point function.

The toy models are not quite as distinguishable. The disk model shows a decidedly higher 2-point function at all but 8 cell LOS separation. The point and filament models, however, are hardly distinguishable at all. This is likely because even though two LOS *can* intersect a single filament, it is unlikely that they will do so in a detectable fashion. First, the only filaments that can be detected as coincidences are those nearly perpendicular to the LOS (otherwise they will either (1) not span the separation of the LOS or (2) the detections will be separated by too large a distance along the LOS to be labeled a coincidence). Of those filaments, it is rather unlikely that two LOS will happen to be oriented to intersect the same filament. On the other hand, to be detected the disks must still be reasonably perpendicular to the LOS, but given that, the probability of

a coincidence is only dependent on the separations of the LOS, and not their relative orientations (because a disk perpendicular to the LOS is two dimensional with respect to the probing LOS). We see that when the separation is one cell and the number density is low (high threshold density; high biasing) the filament model gives a 2-point function clearly distinguishable and between the disk and point models, as expected. While this case *is* at the resolution limit, as mentioned above, in the toy models the shapes were put in by hand (i.e. not evolved with limited force resolution) and the only effect of the grid was the one cell smoothing at the “end”. Therefore, it seems reasonable to be confident that at the high density end (that is, at thresholds that are near the high central densities of the toy shapes and getting away from the smoothing effects), the effects seen are real.

In both the 1 and 2 cell separations, there is a drop in the 2-point function at $0.2\text{--}0.3 \text{ absorbers}/100h^{-1}\text{Mpc}$. Because the point masses aren’t ideal points (once they’re on the grid they occupy a cell of very high constant density, and after smoothing, they are a small cloud, with very high density in one central cell and rapidly decreasing density outside that), they occupy more than one cell, but not by much. This drop in the 2-point function corresponds to a density threshold of $\delta \sim 11$ which is just below the density of the central cell of a single smoothed point mass. Above this density, there can be no coincidences due to a single point mass (but there can be coincidences if two point masses happened to be close together). Thus, the drop is a physical effect of the mesh size.

In general, the toy models seem to be picking out the things expected of them to within the rather low resolution limitations of the grid system imposed on them. Presumably a finer mesh would give better results.

6.3.2 Three-Point Correlation Function Results

First, a reminder: the 3-point function referred to in this section is really ζ_{123} , the *reduced* 3-point correlation function as defined in Eq. 6.9. As such, all 2-

point clustering effects have been removed, so that a non-zero value implies real 3-point clustering effects. The same caveats that applied to the 1 and 8 cell LOS separations in the discussion of the 2-point function apply here as well. The following discussion refers only to the 2 and 4 cell LOS separations unless otherwise noted.

Looking first at the N-body models (Figure 6.9), it can be seen that the $n = -2$ model has a positive and substantially higher 3-point function than the others for $n/100h^{-1} > 1.5$. However, a closer view of the low- n side of the plot (Figure 6.10) reveals that the 3-point function drops *below zero* as well as below the other models for sufficiently high number densities (low density threshold), $n/100h^{-1} < 2$ ($\delta < \sim 1.5$). This effect is probably due to the uneven separations of the LOS. At $S = 1$ cell, the true separations are 1 cell, 1 cell, and $\sqrt{2}$ cells. However, when the 3-point function was calculated (Eq. 6.9), the 2-point function for $S = \sqrt{2}$ cells was not available, and the value for $S = 1$ cell was used instead. Looking at Figures 6.7 and 6.8, it can be seen that there is a substantial difference between the 2-point functions at one and two cell separations for a given number density. Consequently, when the effects of the 2-point function are subtracted, the term corresponding to the $\sqrt{2}$ cell separation is overestimated, and the 3-point function is underestimated. This effect is less at larger separations, as the approximation to an equilateral triangle becomes much better.

Before examining the toy models, let us consider what results we might expect if the 3-point function is indeed able to pick out sheet geometries. The most obvious point is that the disk model should have the highest 3-point function, as it is the only model containing two dimensional structures. Further, the point and filament models are not expected to be distinguishable nor non-zero because neither zero nor one dimensional structures should be seen by the 3-point function.

The 3-point function of the disks (Figures 6.11 and 6.12) is substantially larger than it is for either the filaments or the points, for $n/100h^{-1} Mpc > \sim 1.2$. Be-

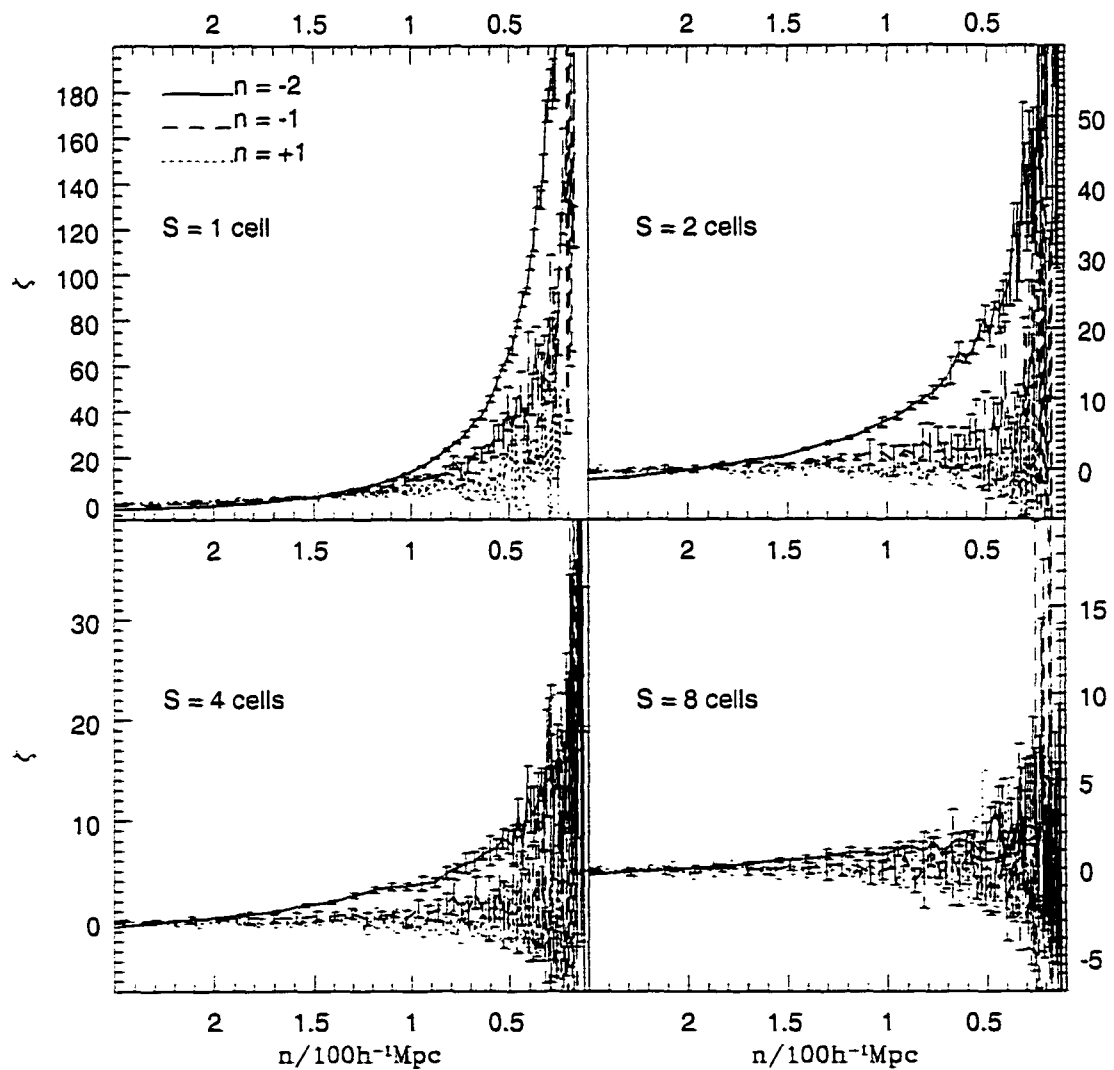


Figure 6.9: The 3-point correlation function for three N-Body models. S is the separation of the LOS in cells. The range of number density of absorbers corresponds roughly to $1.5 \leq \delta \leq 16+$.

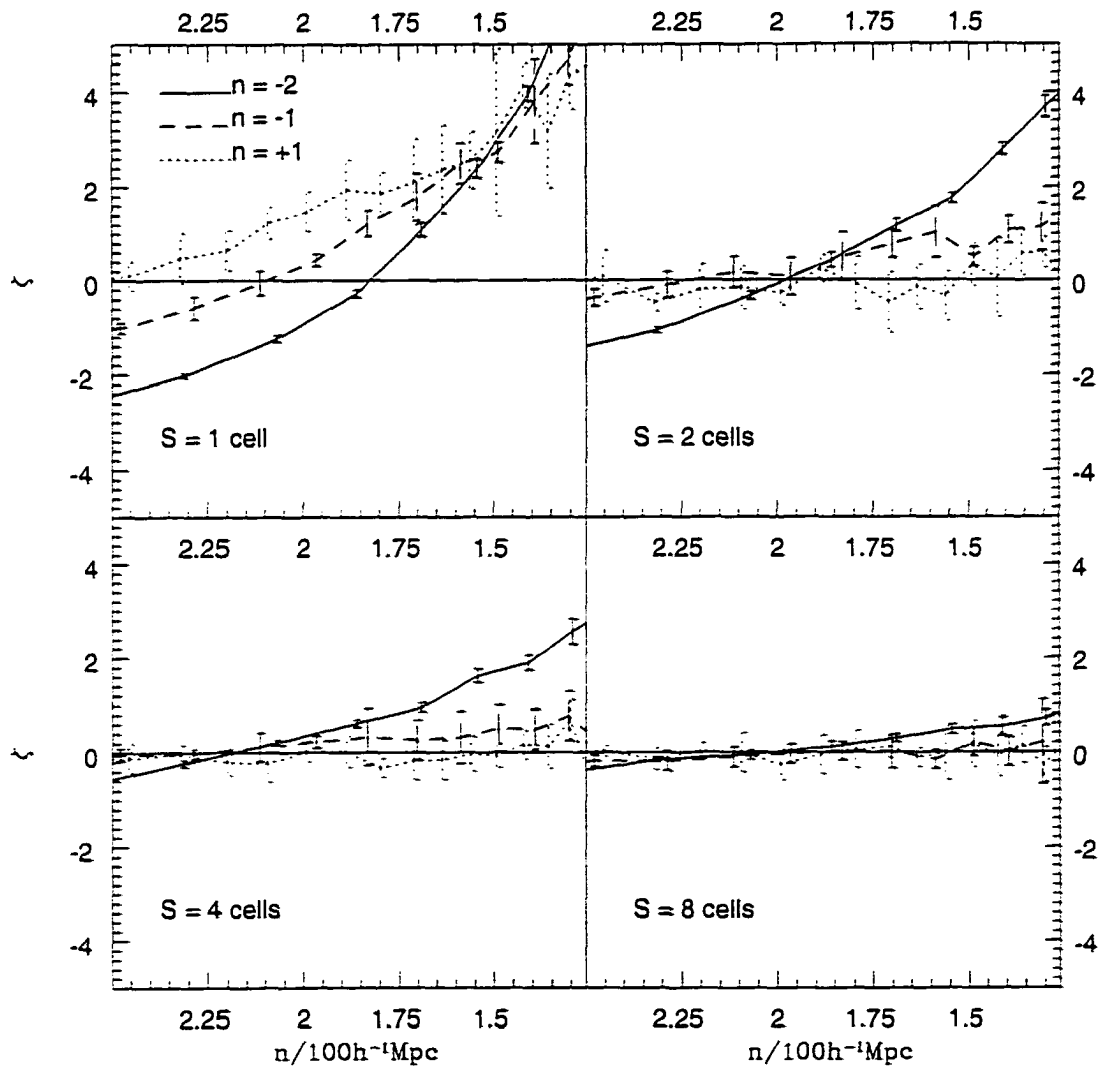


Figure 6.10: A close-up of the 3-point correlation function for the three N-body models shown in Figure 6.6. The range of number density of absorbers corresponds roughly to $1.5 \leq \delta \leq 4$.

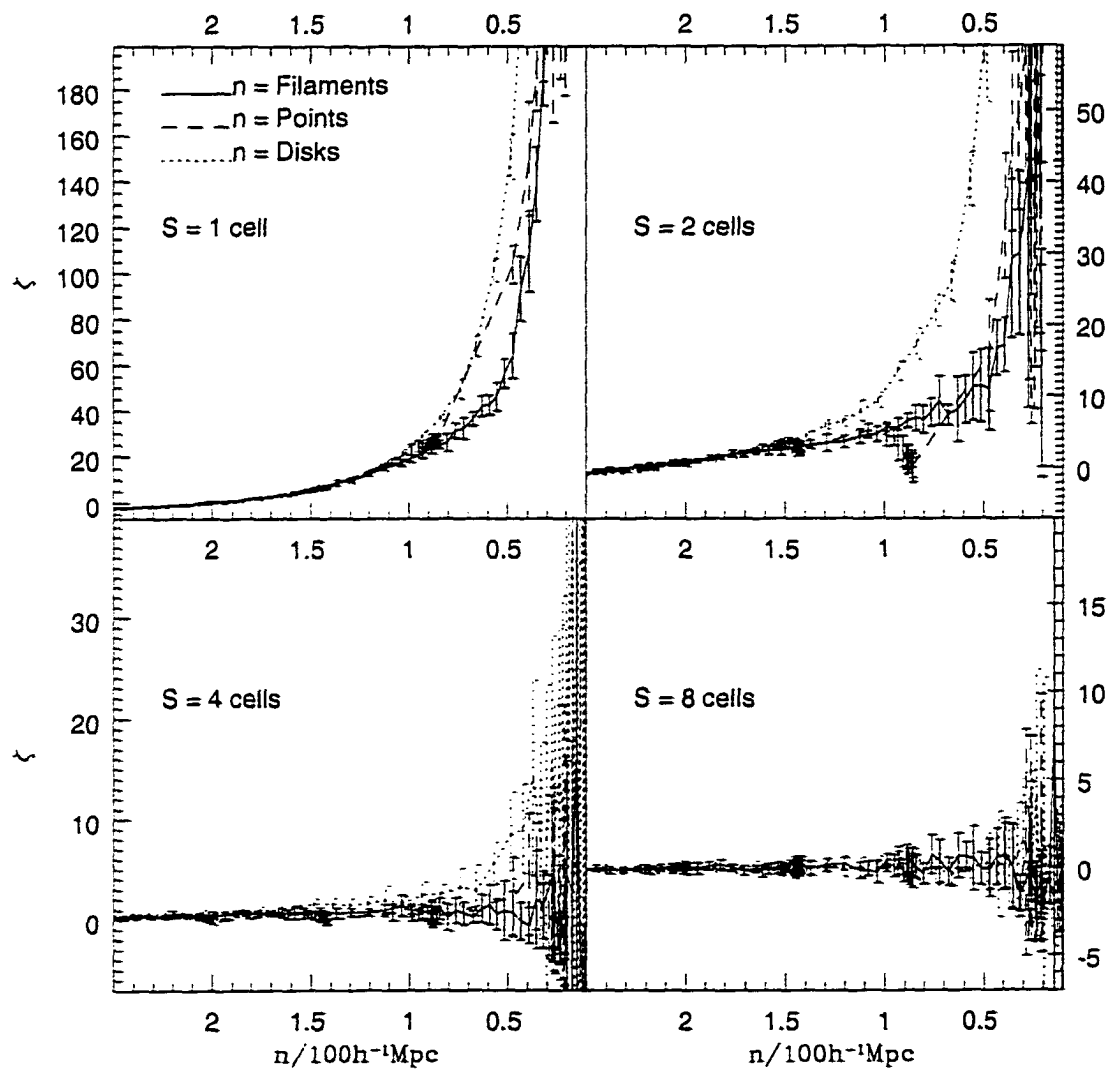


Figure 6.11: As in Figure 6.6 for three toy models. The range of number density of absorbers corresponds roughly to $2 \leq \delta \leq 10$.

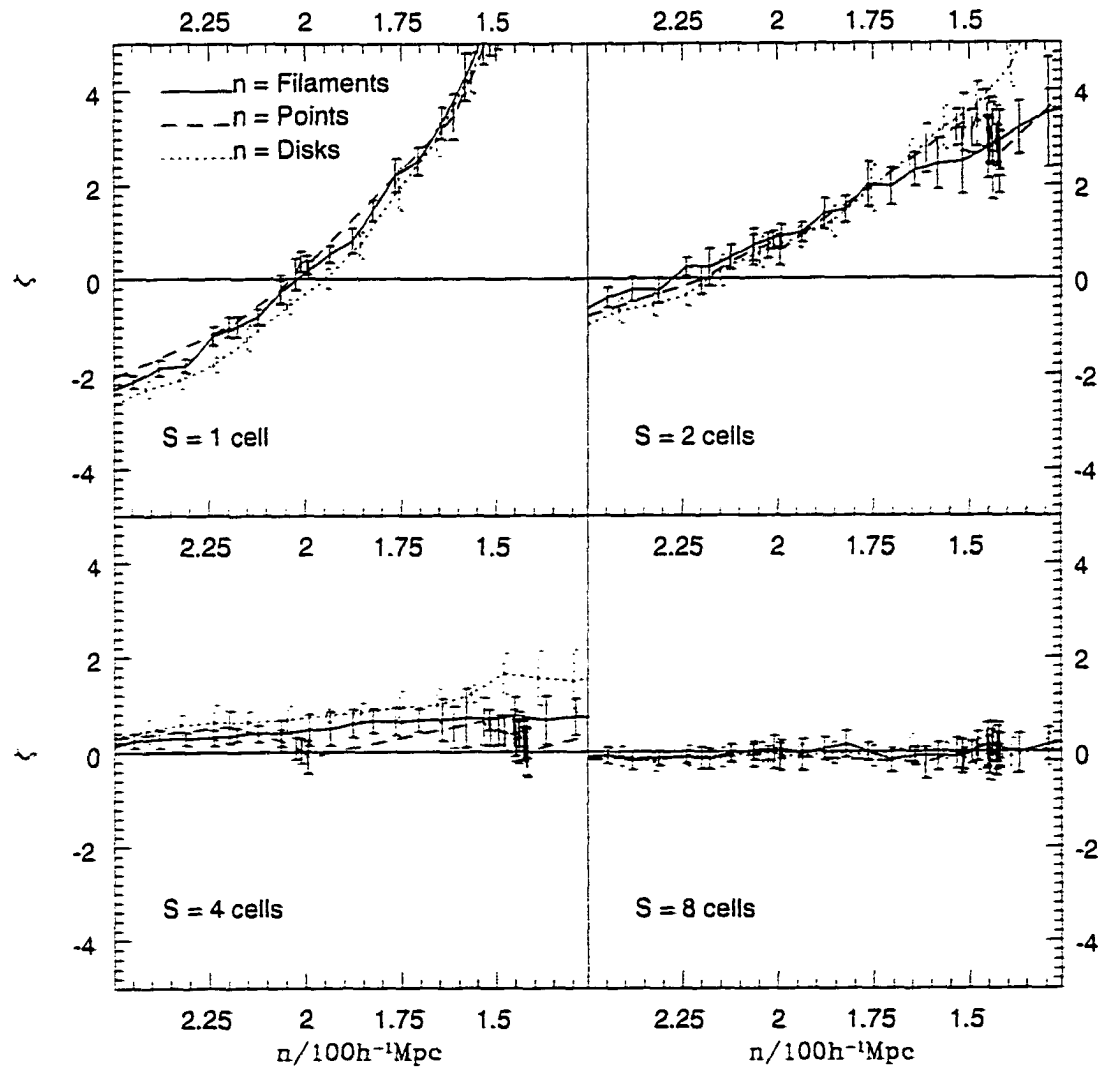


Figure 6.12: A close-up of the 3-point correlation function for the three toy models shown in Figure 6.8. The range of number density of absorbers corresponds roughly to $2 \leq \delta \leq 6$.

low this, all three models are indistinguishable. Presumably this is because the density thresholds are low enough that the absorbers have extended size and the differences between the geometries have been washed out. However, the point and filament models are not distinct anywhere, at any density thresholds (save a small region in the 1 cell separation plot, which is suspect), as expected. However, they do appear to be somewhat non-zero at higher density thresholds. I argue that this is potentially a very minor effect – the error bars are quite large in these regions and nearly include the expected value of zero. Again, at 1 cell LOS separation and low density thresholds, the 3-point function goes negative. The explanation here is the same as for the N-body case. Further work should definitely include toy models with finer meshes and correspondingly smaller smoothing lengths to test these hypotheses.

Additionally, one simple check that can be done is at the 8 cell LOS separation. In all cases the 3-point functions are indistinguishable and zero within error bars. This is what would be expected when the LOS separation is larger than the structures present.

In conclusion, it appears that considering data from three closely-spaced LOS can give a general idea of the geometry of the objects intersected. A positive value of the 3-point function was able to pick out the sheets in the toy models. Point and filament geometries gave relatively very low signals as hoped. This result was also supported by the results from the N-body simulations – there was a distinct positive signal for the $n = -2$ model above the others. This was expected, as that model has a lot of large-scale (and little small-scale) power – the usual recipe for the sheet-like structures known as pancakes. Further work should include a systematic method for extracting the typical sizes of the objects being detected, as well as applying these statistics to real data. Based on the error bars found in the simulations and Lyman-alpha line ranges typical of moderate redshift surveys, I estimate that a sample size of 50-100 such triple-lines-of-sight with a maximum

co-moving separation of about $3 h^{-1} Mpc$ would give a convincing signal. Of course, if the line separations were significantly smaller, there would be less noise and fewer triplets would be needed. Also, if many lines were taken over a small patch of sky, some could be utilized in more than one triplet.

6.4 References

- Bechtold J., Crotts A. P. S., Duncan R. C., & Fang Y. 1994, ApJ, 437, L83
Crotts A. P. S. 1997, preprint, astro-ph/9710295 at <http://xxx.lanl.gov/archive/>
Dinshaw N., Foltz C. B., Impey C. D., Weymann R. J., & Morris S. L. 1995,
Nature, 373, 223
Melott A.L. & Shandarin S.F. 1993, ApJ, 410, 469
Shectman S. A., Landy S. D., Oemler A., Tucker D. L., Lin H., Kirshner R. P., &
Schechter P. L. 1996, ApJ, 470, 172

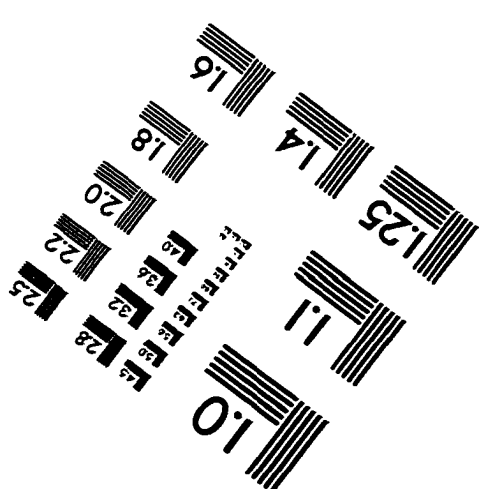
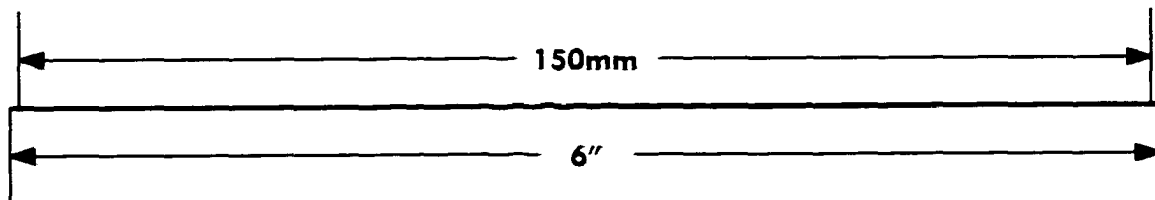
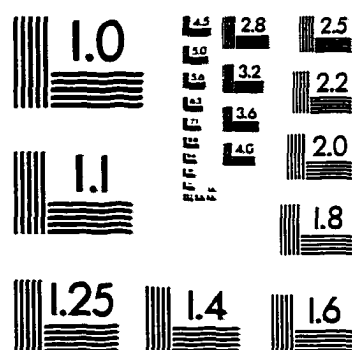
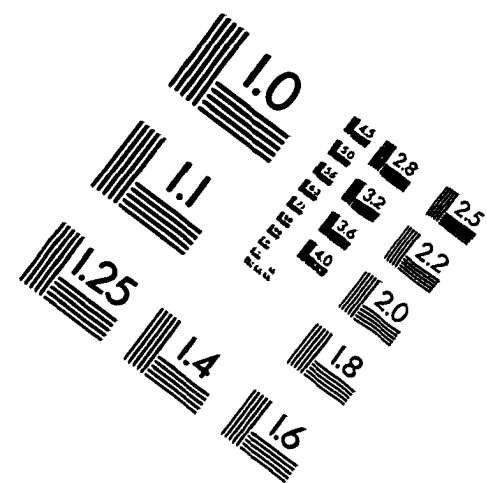
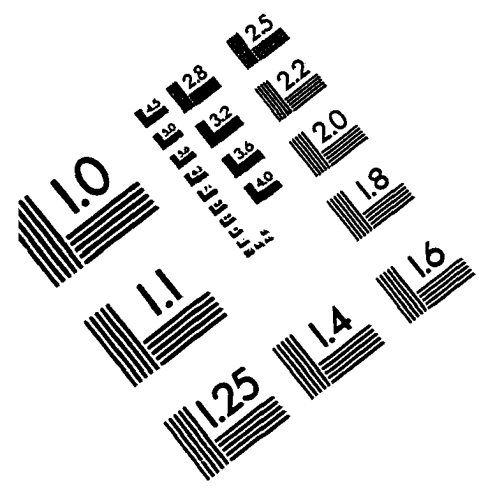
Chapter 7

Conclusions

This body of work focused on the prevalence and importance of sheet-like structures in N-body simulations. I have shown in Chapter 3 that the first objects to collapse tend to be sheet-like. Further, in Chapter 4, I show that objects which form later follow the structure of sheets which is predicted by the truncated Zel'dovich approximation – either directly, or by forming small clumps which flow into a pattern outlining the sheets. My realization that the individual N-body structures were well-described by the Zel'dovich pancakes led me to ask what characteristic of the approximation was responsible for this agreement. In Chapter 5 I show that the answer lies in the similarities of the evolved gravitational potential and the smoothed initial gravitational potential, upon which the TZA is based. This observation suggested a method to improve several existing approximations. One group tested this idea shortly afterward and found it led to marked improvements in the frozen potential approximation. In the final piece of work I developed a statistic capable of detecting sheets using a particular data format very similar to that which could be obtained from the spectra of closely-spaced QSOs. It is my last piece of work which is most open to further research. First, there are refinements which should be made in selecting the separations of the LOS of the 2-point functions for use in calculating the reduced 3-point function.

An improvement in resolution of the simulations would also be helpful, so that I could be confident of the results on the scale of 1-2 Mpc (currently 1 cell LOS separation which is at the resolution limit of the simulation). This statistic, when applied to a data set with a range of LOS separations, also has the potential to give information not only about the geometry, but also about the characteristic sizes of the objects being detected. Since we know, *a priori*, the sizes of the objects in the simulations, it should be possible to calibrate this statistic to give us object size. And finally, this statistic should be applied to real QSO data to determine the sizes and geometry of these large hydrogen structures.

IMAGE EVALUATION TEST TARGET (QA-3)



APPLIED IMAGE, Inc.
1653 East Main Street
Rochester, NY 14609 USA
Phone: 716/482-0300
Fax: 716/288-5989

© 1993, Applied Image, Inc., All Rights Reserved.

